Hurricane Spiral Bands

THOMAS A. GUINN AND WAYNE H. SCHUBERT

Department of Atmospheric Science, Colorado State University, Fort Collins, Colorado

(Manuscript received 4 June 1992, in final form 3 November 1992)

ABSTRACT

The spiral bands that occur in tropical cyclones can be conveniently divided into two classes—outer bands and inner bands. Evidence is presented here that the outer bands form as the result of nonlinear effects during the breakdown of the intertropical convergence zone (ITCZ) through barotropic instability. In this process a zonal strip of high potential vorticity (the ITCZ shear zone or monsoon trough) begins to distort in a varicose fashion, with the potential vorticity (PV) becoming pooled in local regions that are connected by filaments of high PV. As the pooled regions become more axisymmetric, the filaments become thinner and begin to wrap around the PV centers.

It is argued that inner bands form in a different manner. As a tropical cyclone intensifies due to latent heat release, the PV field becomes nearly circular with the highest values of PV in the cyclone center. The radial gradient of PV provides a state on which PV waves (the generalization of Rossby waves) can propagate. The nonlinear breaking of PV waves then leads to an irreversible distortion of the PV contours and a downgradient flux of PV. The continuation of this process tends to erode the high PV core of the tropical cyclone, to produce a surrounding surf zone, and hence to spread the PV horizontally. In a similar fashion, inner bands can also form by the merger of a vortex with a patch of relatively high PV air. As the merger process occurs, the patch of PV is quickly elongated and wrapped around the vortex. The resulting vortex is generally larger in horizontal extent and exhibits a spiral band of PV.

When the formation of outer and inner bands is interpreted in the context of a normal-mode spectral model, they emerge as slow manifold phenomena; that is, they have both rotational and (balanced or slaved) gravitational mode aspects. In this sense, regarding them as simply gravity waves leads to an incomplete dynamical picture.

1. Introduction

A typical hurricane consists of an azimuthally averaged or symmetric flow and asymmetric or banded features. The banded features are often most evident in radar images such as that shown in Fig. 1 (from Gray 1964) and satellite images such as that shown in Fig. 2. From these examples and the numerical integrations performed here, we might conveniently distinguish two types of bands—the inner bands of Fig. 1 and the outer bands of Fig. 2. Inner bands lie close to the vortex center and, while evident on radar images, are often not visible on satellite images because of the cirrus overcast. Outer bands are typically located more than 500 km from the vortex center and can be quite long and narrow.

Since the late 1940s, there have appeared many theoretical papers on hurricane spiral bands. Most of these papers fall into two general classes—the gravity wave theories (e.g., Kurihara 1976; Willoughby 1978) and the boundary-layer asymmetry theories (e.g., Fung 1979; Shapiro 1983). The gravity wave theories, which have been reviewed by Anthes (1982, section 2.3.6), Elsberry et al. (1987, section 2.6.3) and Willoughby (1988), view the spiral bands as regions of upward motion and condensation caused by propagating internal gravity waves. The theories do not agree as to whether the internal gravity waves are forced by convection in the inner regions of the tropical cyclone or by interactions of the outer regions of the tropical cyclone with its environment. The hypothesis of Fung's boundary-layer theory is that bands are produced through dynamic instability of boundary-layer flow structures. In contrast, Shapiro's model does not involve dynamic instability but illustrates how quasi-stationary bands can form in a boundary layer forced by an axisymmetric, moving low pressure pattern. A similar effect is produced by the three-layer tropical cyclone model of DeMaria and Schubert (1984, Fig. 11).

There has been little discussion in the literature about the possibility that hurricane bands are manifestations of PV dynamics, although the above boundary-layer theories could certainly be interpreted in this way. A notable exception is the work of McDonald (1968), who drew attention to qualitative similarities between hurricane asymmetries and planetary-scale Rossby waves. In this paper, we shall argue (sections 2 and 3) that inner bands form through potential vorticity (PV) wave breaking and vortex merging processes. We shall also argue (section 4) that outer bands owe their ex-

Corresponding author address: Dr. Wayne H. Schubert, Department of Atmospheric Science, Colorado State University, Fort Collins, CO 80523.

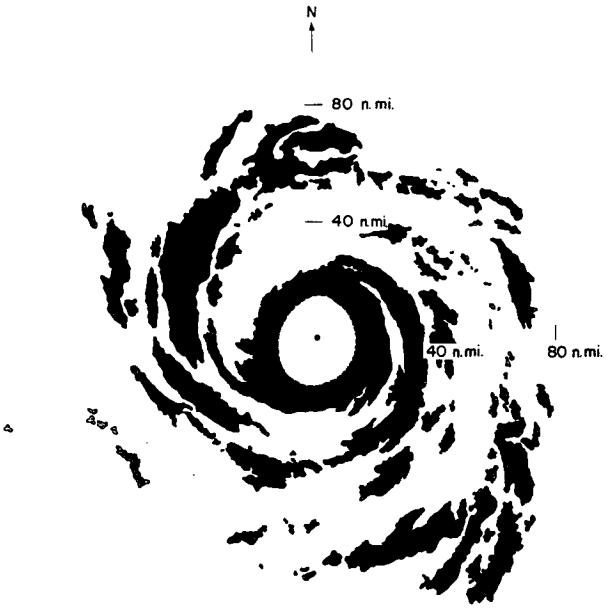

FIG. 1. Radar composite of Hurricane Cleo on 18 August 1958 when it was just east of Bermuda and moving NNE at 7 m s^{-1}. Maximum winds were approximately 47 m s^{-1} and minimum surface pressure 970 mb (from Gray 1964).

istence to the nonlinear potential vorticity dynamics associated with the breakdown of the ITCZ. In a certain sense outer bands are remnants of the ITCZ. The potential vorticity arguments offered here sharply distinguish the present work from previous gravity wave theories of hurricane spiral bands.

The approach adopted here involves numerical simulations with the simplest model that retains both rotational and gravitational modes, that is, an f-plane shallow-water model. We shall simulate features in the potential vorticity field that bear a striking resemblance to the patterns seen in the convective cloud fields of Figs. 1 and 2. Our experience with the shallow-water model indicates that banded features in the PV field are ubiquitous and robust. Since, however, the model is not capable of predicting clouds and the observational data in hurricanes has not yet been used to produce fine grain PV maps, the connection between the model output and the satellite and radar observations remains indirect but suggestive. In particular, it does not seem unreasonable to expect that flow structures that organize the PV in spiral bands can also organize other fields (such as the convective field) into the same bands.

All the numerical integrations described here were performed with the f-plane shallow-water equations

$$\frac{\partial u}{\partial t} - \left(f + \frac{\partial v}{\partial x} - \frac{\partial u}{\partial y}\right)v + \frac{\partial}{\partial x}\left[gh + \frac{1}{2}(u^2 + v^2)\right] = F, \quad (1.1)$$

$$\frac{\partial v}{\partial t} + \left(f + \frac{\partial v}{\partial x} - \frac{\partial u}{\partial y}\right)u + \frac{\partial}{\partial y}\left[gh + \frac{1}{2}(u^2 + v^2)\right] = G, \quad (1.2)$$

$$\frac{\partial h}{\partial t} + \frac{\partial (uh)}{\partial x} + \frac{\partial (vh)}{\partial y} = S, \quad (1.3)$$

on the doubly periodic domain $0 \leq x \leq L_x$, $0 \leq y \leq L_y$. In (1.1)–(1.3), u and v are the eastward and northward components of velocity, h the fluid depth, and F, G, S the effects of friction and mass sources or sinks. In all but one of the experiments presented here, the friction and mass source–sink terms will be set to zero, in which case the system (1.1)–(1.3) possesses the potential vorticity conservation principle $DP/Dt = 0$, where $D/Dt = \partial/\partial t + u\partial/\partial x + v\partial/\partial y$ is the total derivative and $P = (f + \partial v/\partial x - \partial u/\partial y)H/h$ the potential vorticity, with H denoting the constant mean depth of the fluid. The constant factor H is included in the definition of P so that potential vorticity will have the same units as vorticity. With this definition potential vorticity can be interpreted as the vorticity a column of fluid would acquire if the actual depth h were changed to the reference depth H. The numerical method used to solve (1.1)–(1.3) is the normal-mode spectral method described in appendix A.

2. Band formation through wave breaking

We begin by reviewing how the concept of PV (Rossby) wave propagation is tied to the concept of gradients of PV on isentropic surfaces and how, in a nearly symmetric tropical cyclone, the circular isolines of PV (with the highest values of PV in the cyclone center) provide a state on which these waves can propagate.

a. The concept of potential vorticity (Rossby) waves in tropical cyclones

The most elementary treatment of Rossby waves (Platzman 1968) begins with the linearized (about a resting basic state) nondivergent, barotropic, β-plane model in which the northward gradient of basic-state absolute vorticity is the constant β. Under the conservation of absolute vorticity, a sinusoidal disturbance causes fluid particles that are displaced northward to acquire a clockwise spin while fluid particles displaced southward acquire a counterclockwise spin. A fluid particle, which has not been displaced and lies between northward displaced particles to its west and southward displaced particles to its east, will be induced to move southward by the clockwise turning particles to the west and the counterclockwise turning particles to the east. Thus, the whole wave pattern will propagate to the west.

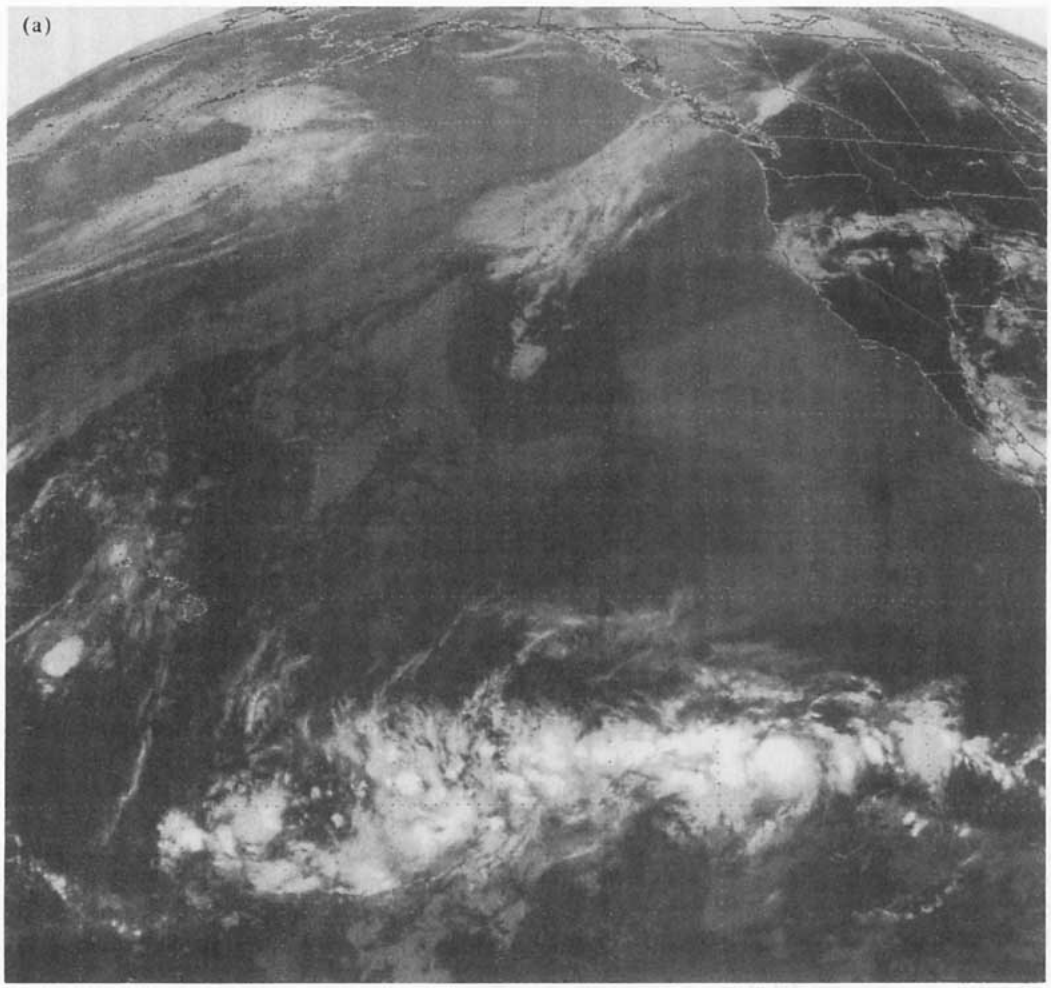

FIG. 2. An example of outer hurricane convective bands. GOES IR images of the eastern Pacific Ocean at 1646 UTC 26 July (a) and 3 August (b) 1988. The striking outer bands emanating from the north and south edges of the tropical cyclone on the left of the 3 August image have formed during ITCZ breakdown and are 1500–2000 km in length.

A more general treatment of Rossby waves (Hoskins et al. 1985, section 6) begins with consideration of the Rossby–Ertel potential vorticity field displayed on an isentropic surface. A reasonable basic state is one in which the isolines of PV are oriented west–east with the higher values of PV to the north. The poleward gradient of PV provides a generalized β effect. If the PV contours (which are also material contours) are perturbed in a sinusoidal fashion, a row of alternating positive and negative PV anomalies is produced. By the invertibility principle (which can take a variety of forms depending on the balance approximation being used) these PV anomalies have an associated flow that further advects the PV field. Just as in the elementary treatment discussed in the previous paragraph, the associated flow makes the PV anomalies propagate westward relative to the basic flow.

In all but the very upper-tropospheric part of an axisymmetric tropical cyclone, the isolines of PV are circles with the highest values of PV found in the center of the cyclone. According to the general argument given in the previous paragraph, this axisymmetric PV field provides a basic state with a monotonic inward increase of PV on which waves can propagate. If the PV pattern is only slightly disturbed from circular isolines, there is a restoring effect and PV wave propagation—the PV contours simply undulate. In certain circumstances, which will be explored shortly, the positive PV anomalies begin to elongate and form spiral tongues of high PV fluid that become thinner and more circular with time. Before exploring this wave breaking process, let us first consider the simplest model of linear PV waves in hurricanes.

We begin with linearized nondivergent barotropic dynamics on a basic-state tangential flow that varies with radius. The basic-state vorticity is assumed to have the top hat form given below in (2.3). The corresponding basic-state streamfunction has the form

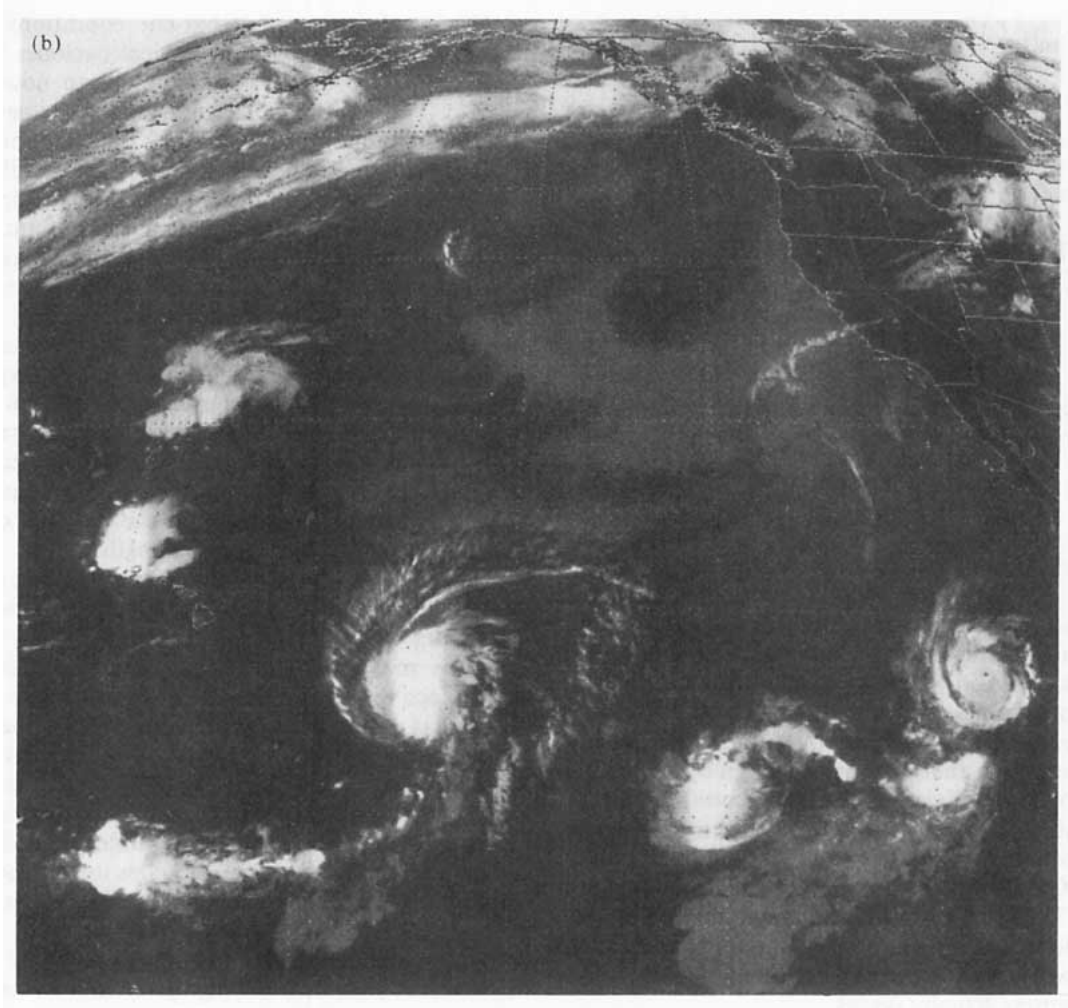

FIG. 2. (*Continued*)

$$\bar{\psi}(r) = \frac{1}{2}\xi\begin{cases}\frac{1}{2}(r^2 - r_1^2), & \text{if} \quad 0 \leq r \leq r_1 \\ r_1^2 \ln(r/r_1), & \text{if} \quad r_1 \leq r < \infty,\end{cases} \tag{2.1}$$

where ξ and r_1 are constants. One differentiation of (2.1) yields the basic-state (Rankine) tangential flow[1]

$$\bar{v}(r) = \frac{d\bar{\psi}}{dr} = \frac{1}{2}\xi\begin{cases} r, & \text{if} \quad 0 \leq r \leq r_1 \\ r_1^2/r, & \text{if} \quad r_1 \leq r < \infty,\end{cases} \tag{2.2}$$

while a second differentiation yields the piecewise constant vorticity pattern

$$\bar{\zeta}(r) = \frac{d(r\bar{v})}{rdr} = \frac{d}{rdr}\left(r\frac{d\bar{\psi}}{dr}\right) = \begin{cases}\xi, & \text{if} \quad 0 \leq r < r_1 \\ 0, & \text{if} \quad r_1 < r < \infty.\end{cases} \tag{2.3}$$

[1] In this paper, the symbols u, v will be used to denote eastward and northward components of velocity when working in Cartesian coordinates and to denote radial and tangential components when working in cylindrical coordinates.

Now suppose the interface between the two vorticity regions is perturbed by an amount $\eta(\phi, t)$ in the sinusoidal fashion $\eta(\phi, t) = \hat{\eta}e^{i(m\phi - \sigma t)}$, where $\hat{\eta}$ is a complex constant, m is the tangential wavenumber, and σ is the frequency. The interface perturbation results in a circular chain of vorticity anomalies. Away from the interface the vorticity is unperturbed from its basic-state value so that $\nabla^2\psi = 0$ for $r \neq r_1$, or, assuming $\psi(r, \phi, t) = \Psi(r)e^{i(m\phi - \sigma t)}$,

$$r\frac{d}{dr}\left(r\frac{d\Psi}{dr}\right) - m^2\Psi = 0 \quad \text{for} \quad r \neq r_1. \tag{2.4}$$

As solutions of (2.4) bounded at $r = 0$ and as $r \to \infty$, we have

$$\Psi(r) = \hat{\psi}\begin{cases}(r/r_1)^m, & \text{if} \quad 0 \leq r \leq r_1 \\ (r_1/r)^m, & \text{if} \quad r_1 \leq r < \infty,\end{cases} \tag{2.5}$$

where $\hat{\psi}$ is a constant that must now be related to $\hat{\eta}$. The continuity of v at $r_1 + \eta$ yields

$$\frac{1}{2}\xi r^2 + m\hat{\psi}\left(\frac{r}{r_1}\right)^m e^{i(m\phi-\sigma t)} = \frac{1}{2}\xi r_1^2 - m\hat{\psi}\left(\frac{r_1}{r}\right)^m e^{i(m\phi-\sigma t)},$$

which, when evaluated at $r_1 + \eta$ and linearized, yields $m\hat{\psi} = -\frac{1}{2}\xi r_1\hat{\eta}$. This is the desired relation between $\hat{\psi}$ and $\hat{\eta}$. The linearized equation governing the movement of the interface is

$$\frac{\partial\eta}{\partial t} + \bar{\omega}\frac{\partial\eta}{\partial\phi} = -\frac{im}{r}\psi, \tag{2.6}$$

where $\bar{\omega}(r)$ is defined by $\bar{v} = r\bar{\omega}$. When (2.5) is used in (2.6) we obtain the dispersion relation

$$\frac{\sigma}{m} = \bar{\omega} - \frac{\xi}{2m} = \frac{1}{2}\xi\left(1 - \frac{1}{m}\right). \tag{2.7}$$

Thus, wavenumber $m = 1$ is stationary and wavenumbers $m = 2$, 3, 4 move, respectively, at 1/2, 2/3, and 3/4 the speed of the basic-state tangential flow.

The above analysis demonstrates that a vortex generally possesses a restoring mechanism that opposes departures from axisymmetry. This is often referred to by meteorologists as the Rossby restoring mechanism. Since the above analysis was first given by Sir William Thomson (Lord Kelvin) in 1880 and was summarized by Lamb (1932, pp. 230–231), attributing the origin of this concept to Rossby (1939) is not historically accurate. Calling the waves obeying the dispersion relation (2.7) Kelvin waves, however, would be confusing for obvious reasons. Here we shall refer to these waves as PV waves, or more conventionally but less accurately, simply Rossby waves.

b. *Evolution of noncircular PV distributions—wave breaking and surf zones*

Now we shall describe a flow evolution that culminates in PV wave breaking. Since PV is materially conserved the entire process is simply an advective rearrangement of PV. This concept of wave breaking was first introduced for theoretical work by Deem and Zabusky (1978a,b) and Zabusky et al. (1979) in their contour dynamics studies of finite area vortex patches and for observational work by McIntyre and Palmer (1984, 1985) in their analysis of the extratropical middle stratosphere. Numerical simulations of Rossby wave breaking were later presented by Juckes and McIntyre (1987). In these studies, a representative isentropic surface in the stratosphere was divided qualitatively into two distinct regions—the *main vortex,* described as an area of high PV with sharp PV gradients at its edge, and the *surf zone,* an area where systematic large-scale PV gradients are comparatively weak. The name *surf zone* implies a region where PV wave breaking occurs repeatedly.

Having demonstrated that the conditions for PV wave propagation exist in tropical cyclones (section 2a), the concept of wave breaking can now be discussed. McIntyre and Palmer (1985) envisaged wave breaking as the *rapid, irreversible* deformation of material contours. For adiabatic and frictionless flows, the material contours in question are simply isopleths of PV. Wave breaking in this context is important because it often determines whether PV waves will make quasi-permanent changes to the mean flow in which they are embedded. The word *rapid* in the context of wave breaking implies the time scale of the material disturbance should not be much longer than a typical intrinsic wave period in the area of interest but should also be much shorter than dissipative time scales. The word *irreversible* is used in a sense similar to that in statistical mechanics, that is, an irreversible process is one in which small changes in the material contours cannot be made to retrace their path.

It should also be noted that wave breaking does not imply that instabilities exist in the flow. Although instabilities can be important in certain cases, the irreversible material deformations discussed above can take place in the absence of any recognizable instabilities. It is often the wave breaking process that causes instabilities and not vice versa. Finally, it should be remembered that the concept of wave breaking is not an exact diagnostic tool. There are no mathematical formulas or specific patterns that uniquely define wave breaking. The concept is nonetheless useful when trying to understand the complex nature of wave–mean flow interactions.

Although tropical cyclones are considerably different in terms of scale and forcing mechanisms from stratospheric planetary waves, the concept of wave breaking is also of considerable use in examining the evolution of spiral bands in tropical cyclones. The dynamical similarity occurs because tropical cyclones also contain a main vortex surrounded by a surf zone in which the spiral bands are found. In this context, the wave breaking process can be thought of as modifying the mean wind profile by ejecting high PV air downgradient into regions of relatively low PV.

A numerical experiment will now be set up to illustrate PV wave breaking in our shallow-water model. For this experiment we have chosen a square domain 1600 km on each side with a spectral truncation limit of $M = N = 84$ and with 256×256 points on the transform grid. The mean fluid depth is $H = 300$ m, giving a gravity wave speed of $c = (gH)^{1/2} = 54.2$ m s^{-1}. The Coriolis parameter is chosen to be 5.0×10^{-5} s^{-1}, corresponding to approximately 20°N which yields a Rossby length c/f of 1084 km. With these choices the centers of adjacent vortices, which implicitly surround the vortex in question because of the periodic boundary conditions, are approximately 1.5 Rossby lengths away. To avoid resolution problems, we shall specify initial disturbances that are somewhat larger than would be

expected in real tropical cyclones. This does not alter the fundamental dynamics.

The initial condition consists of vorticity isopleths that are concentric ellipses sharing the same orientation and aspect ratio. This particular pattern, taken from Melander et al. (1987a), was chosen to represent essentially wavenumber 2 asymmetries. The initial mass field was determined from the initial flow field using the nonlinear balance equation $g\nabla^2 h = f(\partial v/\partial x - \partial u/\partial y) + 2\partial(u, v)/\partial(x, y)$. Figure 3a shows the initial fields for this experiment. A maximum value of 5.0×10^{-4}, or $10f$, was chosen for the relative vorticity. Note that only the inner 800 km × 800 km area is shown. Figures 3b–d show the time evolution of the fields at 6-hour intervals. By 6 h, wave breaking has begun. The wave breaking process can be crudely understood by noting that the flow remains quasi-balanced and that inversion of the PV field to obtain the wind field is a smoothing operation. The winds are therefore more axisymmetric than the corresponding PV field. Then cross-contour flow distorts the PV contours, resulting in wave breaking. More detailed interpretations of the wave breaking and axisymmetrization process in terms of a corotating streamfunction are given in Melander et al. (1987a) and Polvani et al. (1989). During wave breaking, mass is actually removed from the high PV region, and the PV gradient begins to steepen. This is especially evident in the lower right quadrant of the domain. By 12 h the region of steep PV gradient nearly encircles the main vortex. This process continues until 24 h, at which time the gradients have become too steep for the model to resolve and the Gibbs phenomenon begins to occur. Filaments such as those shown in Fig. 3d might be expected to roll up into smaller eddies. The effects of strain and adverse shear tend to prevent such rollup, however, as pointed out in the recent work of Dritschel (1989), Dritschel et al. (1991), and Waugh and Dritschel (1991).

There is a certain dynamical analogy between the PV wave breaking processes occurring in tropical cyclones and those occurring in the wintertime stratosphere, even though the horizontal length scales and wave excitation mechanisms are quite different. In the wintertime stratosphere, there exists a polar vortex with a large PV gradient at its edge. Quasistationary Rossby waves, excited in the troposphere, can propagate upward along the edge of this polar vortex and lead to wave breaking in the stratosphere. Similarly, a tropical cyclone vortex is a region of high PV with a large PV gradient at its edge. A variety of processes can conspire to make the high PV region less axisymmetric, that is, to excite PV waves on the vortex edge. In the natural tendency of the vortex to return to axisymmetry, the banded features characteristic of breaking Rossby waves are produced in the surf zone surrounding the vortex. Among the processes that can lead to asymmetry in the PV distribution, one might expect asymmetry in the moist convection to be of importance since the high PV in the vortex center has been induced by moist convection. Another means of producing inner vortex asymmetries in real tropical cyclones, suggested to us by K. Emanuel (personal communication), is as follows. Even with weak background vertical shear, the upper-level anticyclone, which is not remotely axisymmetric, is displaced away from the surface cyclone. The subsequent interaction of these upper- and lower-level PV anomalies will produce asymmetric structure in the lower vortex. If these asymmetry-producing processes (whatever their cause) and the PV wave breaking process are fairly continuous in time, we might expect the surf zone to become (as Melander et al. 1988 term it) a tangle of nearly concentric PV filaments.

c. *Lagrangian trajectory analysis and wave activity diagnostics*

The normal-mode shallow-water model used in the above experiment has incorporated into its code the option of also predicting the movement of two passive scalars $\alpha_i(x, y, t)$ $(i = 1, 2)$, that is, of solving $D\alpha_i/Dt = 0$ along with the three equations of the shallow-water model. These passive tracers are useful for studying Lagrangian trajectories in the banding process. This can be accomplished by initializing the two tracer fields by $\alpha_1(x, y, 0) = \sin(2\pi x/L_x)$ and $\alpha_2(x, y, 0) = \sin(2\pi y/L_y)$ so that the isolines of $\alpha_1(x, y, 0)$ are parallel to the y axis and the isolines of $\alpha_2(x, y, 0)$ are parallel to the x axis, as shown in Fig. 4 for the inner 800 km × 800 km of the computational domain. A Lagrangian particle trajectory can then be obtained by following the movement of a particular pair of intersecting α_1 and α_2 isolines. Similarly, a finite size parcel of fluid can be traced by following the region that remains bounded by the same two α_1 contours and the same two α_2 contours. The movements of four parcels that began approximately 250 km from the vortex center are followed for 6 hours in Fig. 4. The two parcels starting on the major axis have higher PV and are folded inside the two parcels with smaller PV. In this way the PV distribution becomes more symmetric.

For those readers familiar with the wave activity concepts arising in wave–mean flow interaction theory, maps of wave activity and its flux (Fig. 5) have been produced for the wave breaking experiment shown in Fig. 3. A derivation of the wave activity relation and a discussion of Fig. 5 can be found in appendix B.

If the wave breaking experiment shown in Fig. 3 is repeated with more and more circular initial vorticity distributions, the onset of wave breaking is delayed. Using a single-contour version of the contour dynamics/contour surgery approach, Polvani and Plumb (1992) have demonstrated how, even in the absence of wave breaking, tracer distributions outside the vortex are disrupted. Thus, some banding of passive scalars is possible, even in the absence of wave breaking, if the inner PV region is somewhat asymmetrical.

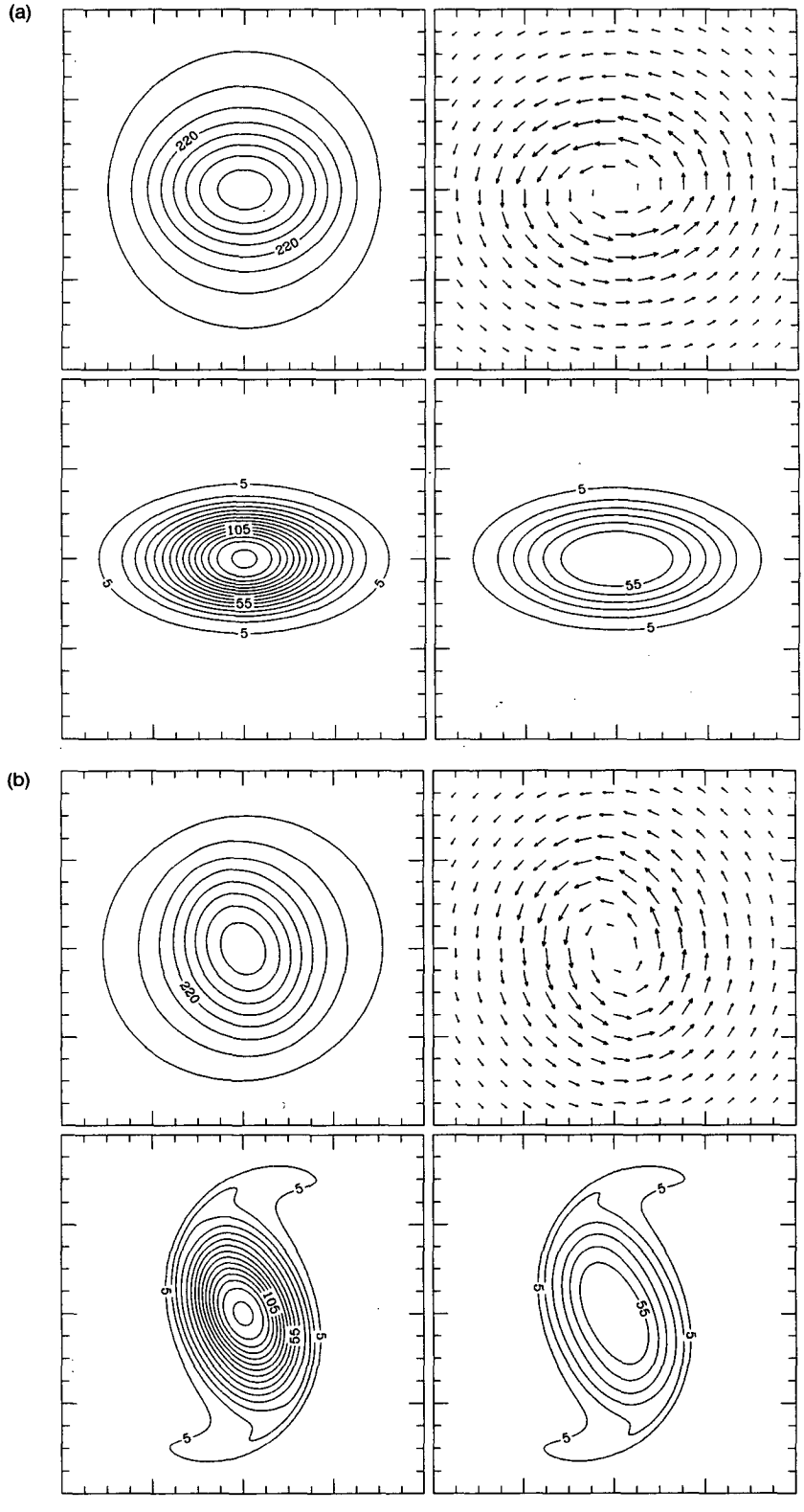

FIG. 3. Dynamic fields for experiment 1 at (a) initial time, (b) 6 h, (c) 12 h, (d) 18 h. Upper left panel of each set shows the fluid depth with a contour interval of 20 m, upper right panel the horizontal winds, lower left panel the potential vorticity, and lower right panel the absolute vorticity. Potential vorticity and absolute vorticity are in units of 10^{-5} s^{-1} and have contour intervals of 10^{-4} s^{-1}. The displayed domain is 800 km $\times$ 800 km, with tick marks every 50 km. The initial wind and mass fields satisfy the nonlinear balance equation.

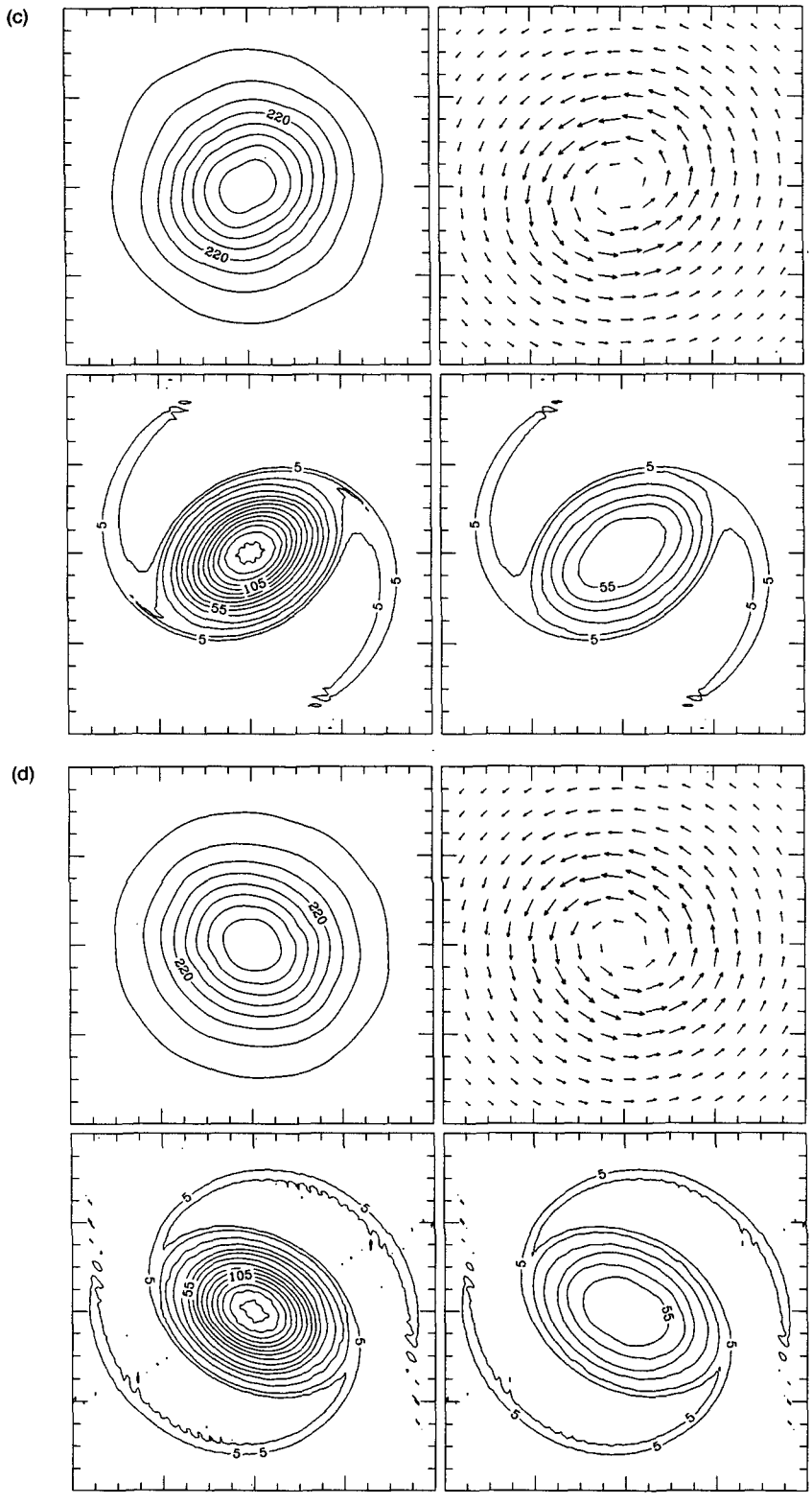

FIG. 3. (*Continued*)

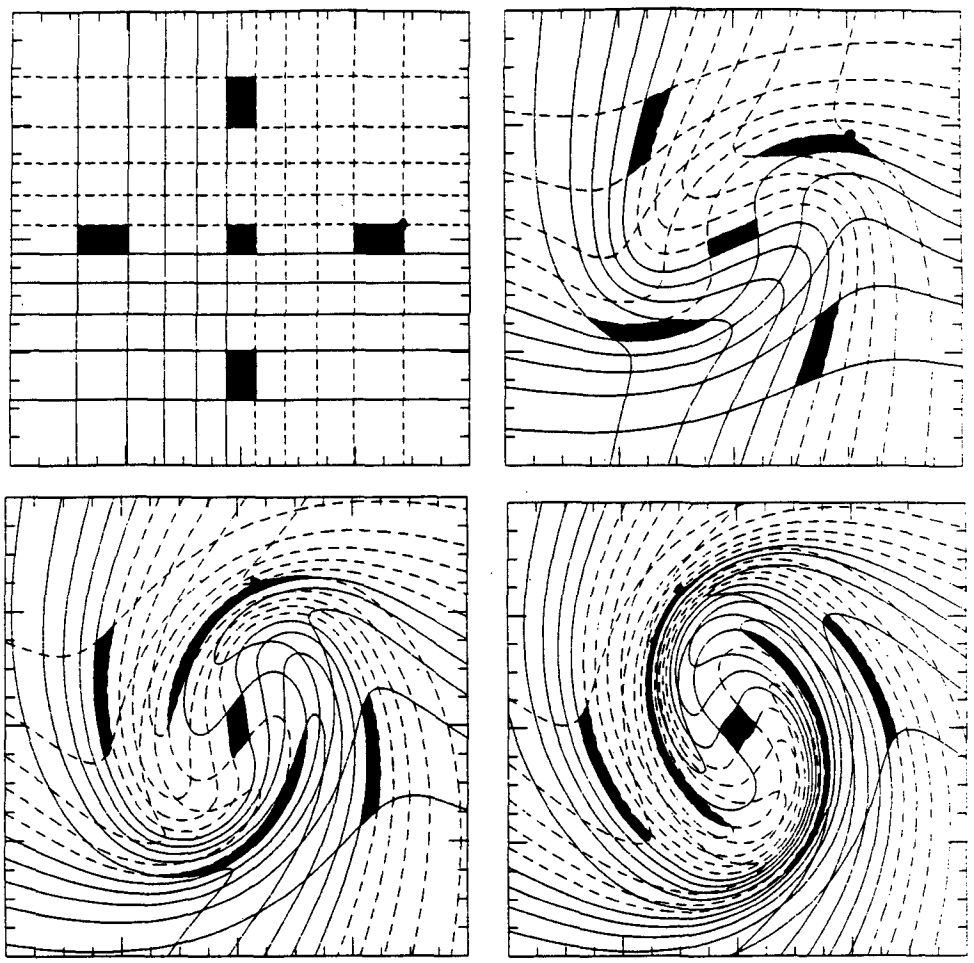

FIG. 4. Lagrangian parcel trajectories for experiment 1. Four marked parcels are initially (upper left) equal distances from the vortex center. Subsequent positions at 2 h (upper right), 4 h (lower left), and 6 h (lower right) illustrate how the two parcels originating on the major axis of the elliptical PV pattern are folded inside the two parcels originating on the minor axis.

d. Are bands gravity waves?

As noted in appendix A, the normal-mode spectral method provides a natural partitioning of the total solution into rotational and gravitational parts. This is accomplished by simply dividing the total sum on the right-hand side of (A.5) into two partial sums, one over the rotational modes ($q = 0$) and one over the gravitational modes ($q = 1, 2$). The top panels of Figs. 6 and 7 show the total geopotential, wind, and vorticity at 12 h for the wave breaking experiment. The lower panels show the partition of these total fields into rotational and gravitational parts. As can be seen in Fig. 6, the wind field is composed almost entirely of rotational modes, while the geopotential field is composed of both rotational and gravitational modes, with the gravitational modes contributing that part of the geopotential that takes us from geostrophic to gradient balance. Consistent with Fig. 6, we note that the banded features in Fig. 7 are not due to gravity modes but are composed almost entirely of rotational modes.

The natural partitioning provided by the normal-mode model leads directly to Leith's (1980) schematic manifold diagram (Fig. 8), in which the axes R and G denote the rotational and gravitational linear manifolds, with R consisting of all linear combinations of eigenfunctions associated with the low-frequency rotational modes and G consisting of all linear combinations of eigenfunctions associated with the high-frequency gravitational modes. Since the eigenfunctions are individually orthogonal, R and G are orthogonal. In addition, since the eigenfunctions form a complete set, any model state can be represented schematically by a point in the manifold diagram.

For flow fields in which the transient adjustment processes have had time to establish a quasi-balanced state, the time evolution tends to be along a slow manifold, one definition of which is obtained by dividing

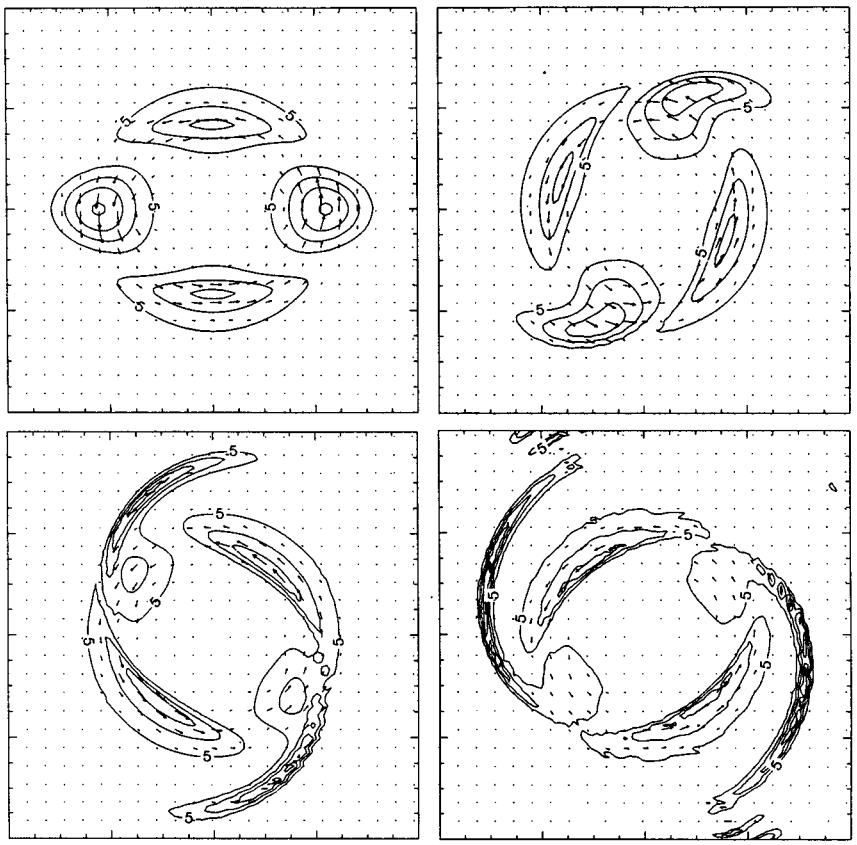

FIG. 5. Wave activity and its flux at 4-hour intervals for experiment 1. Times are 0 h (upper left), 4 h (upper right), 8 h (lower left), and 12 h (lower right). Centers of wave activity starting on the minor axis change only slightly while centers starting on the major axis are rapidly elongated into bands.

the predictive equations [see appendix A, Eq. (A.7)] for the normal-mode spectral coefficients $W_{mnq}(t)$ into the slow-mode class ($q = 0$) and the fast-mode class ($q = 1, 2$) and then treating the fast-mode class diagnostically, that is,

$$\frac{dW_{mn0}}{dt} = N_{mn0} + F_{mn0}, \tag{2.8a}$$

$$i\nu_{mnq}W_{mnq} = N_{mnq} + F_{mnq} \quad (q = 1, 2). \tag{2.8b}$$

Here N_{mnq} and F_{mnq}, respectively, represent the projections of the nonlinear and forcing terms onto the normal mode having the integer m as its x wavenumber, the integer n as its y wavenumber, and ν_{mnq} as its frequency. In simulating slow manifold evolution, the normal-mode equations for slow (rotational) modes are treated prognostically by (2.8a) while the normal-mode equations for fast (gravitational) modes are treated diagnostically by (2.8b). From (2.8) we can envision two slow manifolds. If diabatic and frictional effects are neglected so that F_{mnq} ($q = 0, 1, 2$) vanishes, (2.8) defines the adiabatic, frictionless slow manifold given by the lower curve in Fig. 8. If diabatic and frictional effects are included, the divergence patterns should be stronger and the projection of the total solution onto G should be larger. This diabatic, frictional slow manifold is given by the upper curve in Fig. 8. The model results shown in this paper are for the shallow-water primitive equations but they correspond closely to evolution along the adiabatic frictionless slow manifold.

From Fig. 8 one can think of the gravitational-mode contribution to the total solution as consisting of three parts. The first part takes us from the R axis to the adiabatic, frictionless slow manifold, that is, from a geostrophically balanced flow to a higher-order (gradient type) balanced flow. The second part takes us from the adiabatic, frictionless slow manifold to the diabatic, frictional slow manifold, that is, to flow patterns with significant convergence and associated moist physical processes. The third part is the transient part of the gravitational-mode contribution, that is, that part that is not in balance with nonlinear advection and diabatic and frictional effects. This transient part tends to be quite small if the diabatic processes evolve slowly in time. As discussed by Schubert and DeMaria (1985), it is only the third part that is missing in balanced models such as the Eliassen balanced vortex model.

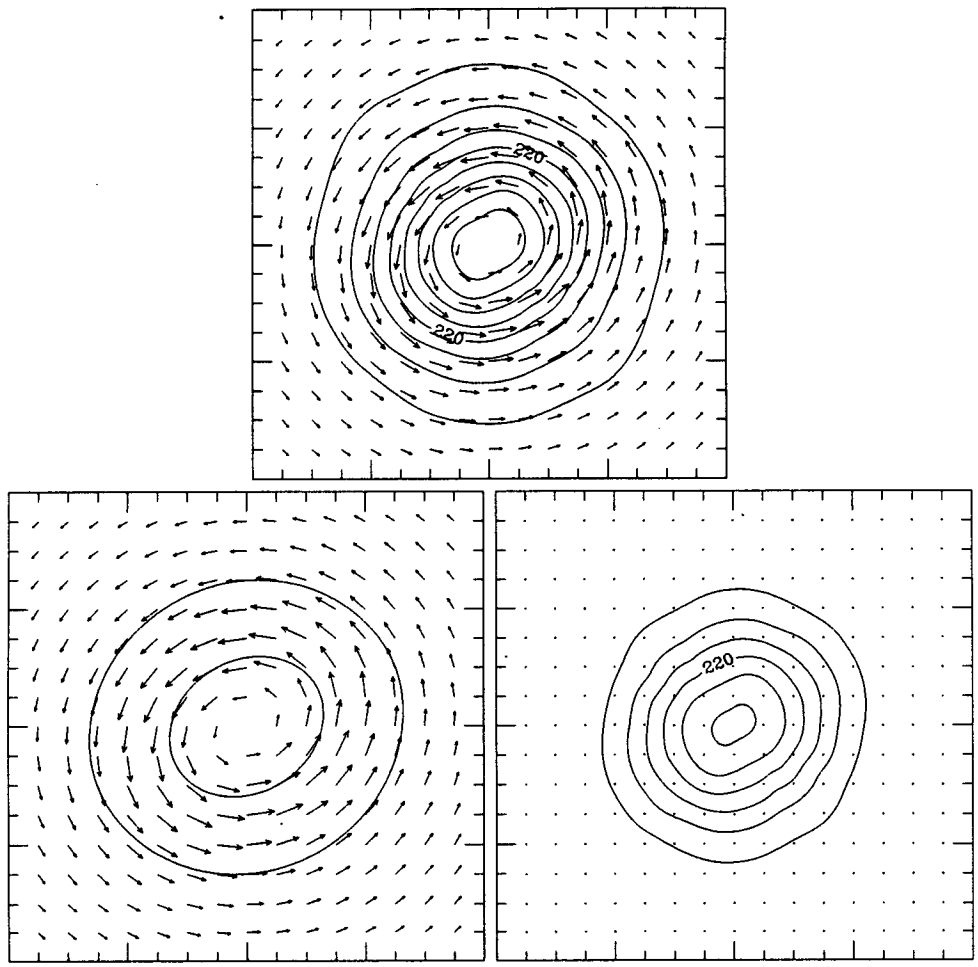

FIG. 6. Rotational (lower left) and gravitational (lower right) mode contributions to the total (upper) wind and mass fields at 12 h for experiment 1. Contour intervals are the same as in Fig. 3.

This discussion can be summarized by noting that Figs. 6 and 7 show that bands forming during model evolution along the adiabatic frictionless slow manifold have little contribution from gravitational modes. This suggests the possibility that real tropical cyclone spiral bands may be primarily rotational, slow manifold phenomena. The bands in real tropical cyclones however, do not evolve along the adiabatic, frictionless slow manifold, so that our model underestimates the real gravitational-mode contributions. Further understanding of tropical cyclone bands could no doubt be obtained with more general models that include vertical structure and moist physical processes, such as the model recently developed by Shapiro (1992).

3. Band formation through vortex merger and diabatic sources away from the cyclone center

a. Vortex merger

In the previous section, the formation and evolution of inner bands through wave breaking processes has been considered. We now demonstrate how spiral bands can also be formed when a preexisting cyclonic vortex merges with a region of enhanced PV. Vortex merger is not a new concept. Although it has been examined in numerous fluid dynamical studies (e.g., Fornberg 1977; McWilliams 1984; Griffiths and Hopfinger 1987; Melander et al. 1987a,b, 1988), its application to tropical cyclones has only recently begun with the observational work of Holland and Lander (1993) and Lander and Holland (1993), the contour dynamics study of Ritchie and Holland (1993), and the barotropic model study of Holland and Dietachmayer (1993).

When a cyclonic vortex moves sufficiently close to another cyclonic vortex of equal intensity, the two vortices may merge or coalesce to form a larger vortex. Extending from the newly formed vortex will be spiral arms of relatively high vorticity. This process has been elegantly illustrated in laboratory experiments by Griffiths and Hopfinger (1987). If the vortices are not sufficiently close to one another, they may simply rotate

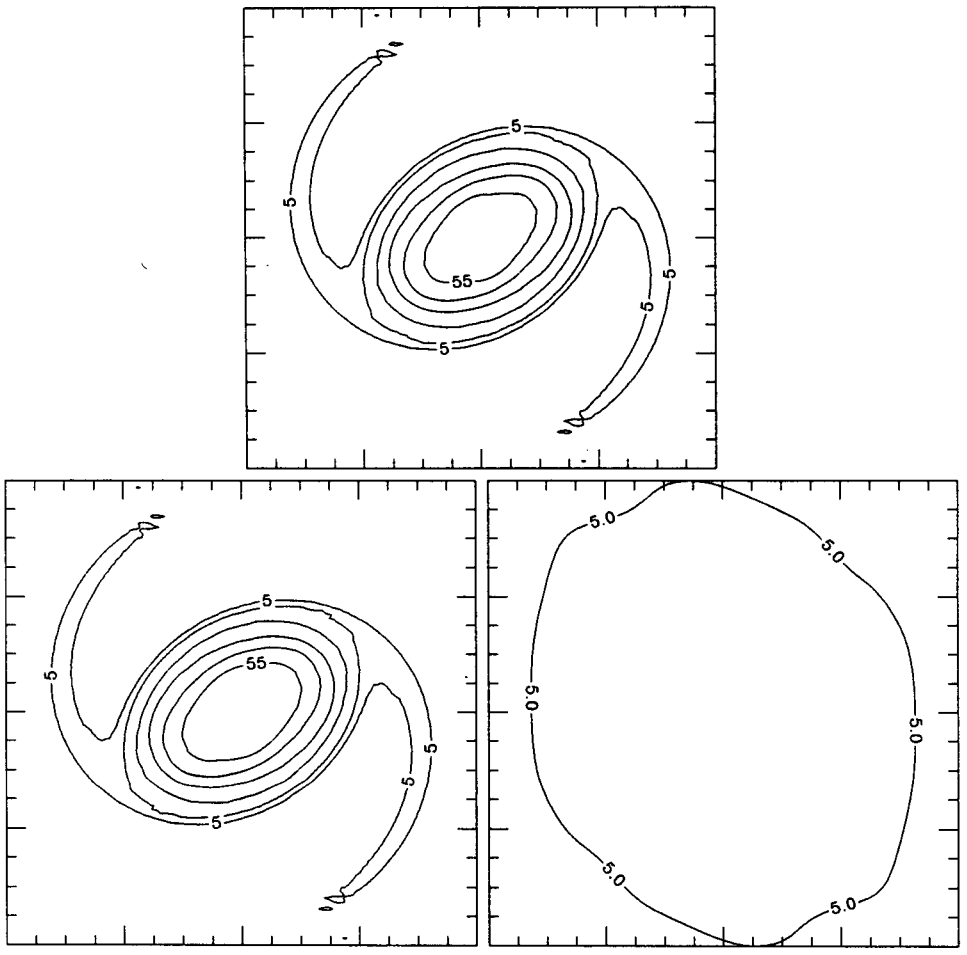

FIG. 7. Rotational (lower left) and gravitational (lower right) mode contributions to the total (upper) vorticity at 12 h for experiment 1. Contour intervals are the same as in Fig. 3.

around one another without merging (Fujiwhara 1923), or they may move apart. Of greater importance to hurricane spiral bands is the merger of vortices having different intensities. In this section, three vortex merger experiments will be considered, all of which produce spiral bands in the PV field. The first two (experiments 2 and 3) retain 108 waves and use a transform grid with $(256)^2$ points. Although quadratically nonlinear terms are not alias free, results indicate that for relatively short model integrations ($\sim$1 day), the increased resolution outweighs any problems associated with aliasing error.

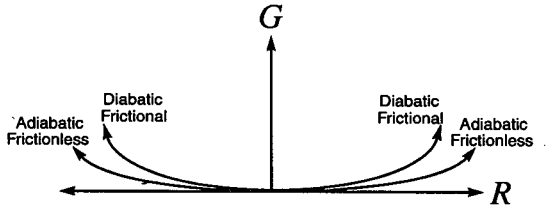

FIG. 8. Leith's (1980) schematic slow manifold diagram: R denotes the rotational linear manifold and G the gravitational linear manifold. Adiabatic, frictionless, quasibalanced flow evolution (such as that found in our shallow-water model integrations) tends to be along the lower slow manifold. Diabatic, frictional, quasi-balanced flow evolution (such as that found in real tropical cyclones) tends to be along the upper slow manifold.

Experiment 2, which is shown in Fig. 9, involves the interaction of an intense vortex with a weaker vortex of similar size. The left vortex was initialized with a maximum vorticity three times that of the right vortex. As the vortices evolve, the differential rotation associated with the more intense circulation rapidly acts to deform the weaker vortex, whereas the circulation associated with the weaker vortex has only a slight impact on the more intense vortex. By 24 h, the weaker vortex has been stretched and advected around the stronger vortex, yielding a single spiral band of PV.

In experiment 3, a strong, small vortex that encounters a larger, weaker vortex is considered. This case is analogous to a hurricane that forms near a large,

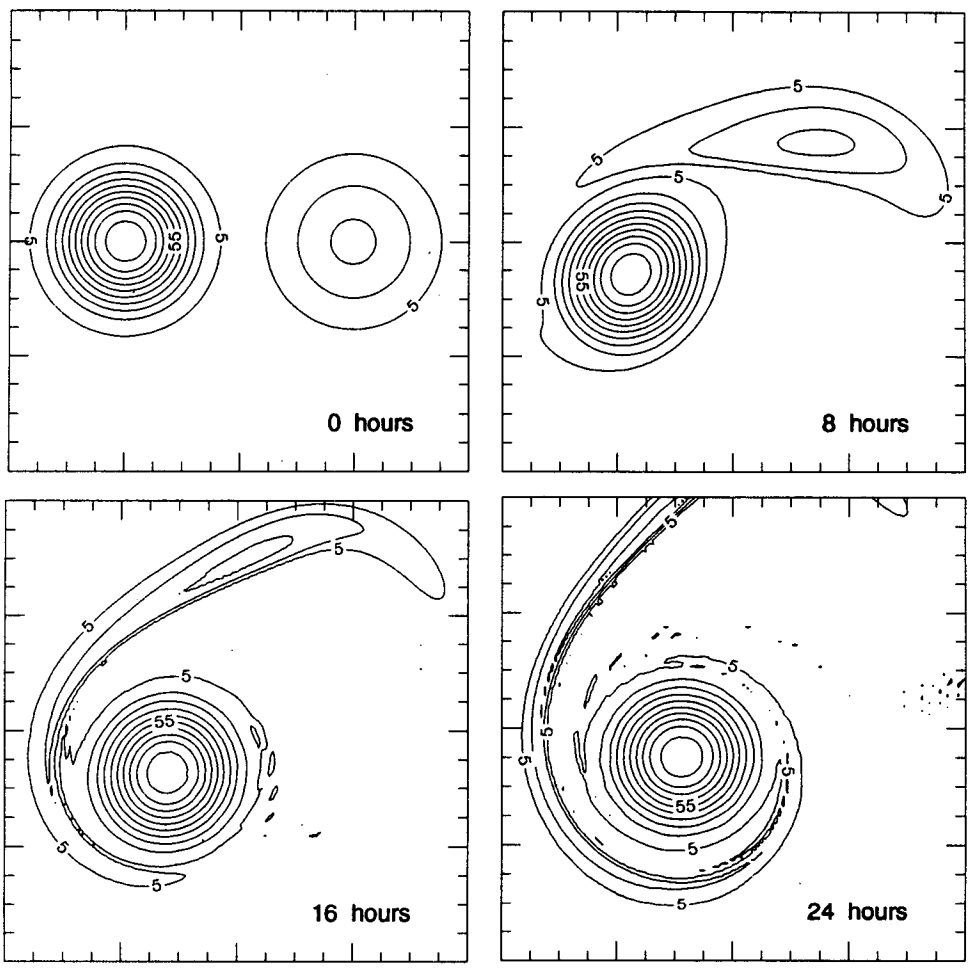

FIG. 9. Experiment 2: merger of two equally sized vortices of different intensities. The four panels display the PV field at 0, 8, 16, and 24 h. The left vortex was initialized with a maximum vorticity three times that of the right vortex. Units are 10^{-5} s^{-1}.

amorphous monsoon trough. Figure 10 shows the evolution of the PV field for this simulation. The initial vorticity of the small vortex has a maximum value that is three times that of the larger vortex. As the flow evolves, the wind field associated with the small intense vortex stretches the PV field of the large vortex. By 24 h, much of the PV initially associated with the large vortex surrounds the smaller vortex. The remainder of the larger vortex appears as a wide band with a sharp bend approximately 500 km south of the vortex center. Similar sharp bends in the convective bands of real tropical cyclones have been noted by Lewis and Hawkins (1982). The final result of this merger is a region of PV with approximately four times the area of the original small intense vortex. This may help explain the large variation in the size of tropical cyclones (Merrill 1984). An argument recently advanced by G. Holland (personal communication) goes as follows. If a tropical cyclone forms near the monsoon trough, it could be provided with a relatively large pool of PV from which to grow. If a tropical cyclone forms away from such a PV source, it would be expected to remain smaller in size. This argument will be further examined in the next simulation.

For experiment 4, the effect of placing a vortex near a strip of enhanced PV is considered. This experiment is performed using $(128)^2$ points on the transform grid and retaining 42 waves. It is intended to simulate the effect of tropical cyclone formation near the edge of a zonally elongated monsoon trough. Figure 11 shows the PV field for this simulation at 0, 16, 32, and 48 h. The cyclonic circulation associated with the vortex acts to advect relatively high PV air from the strip northward on the east side of the vortex and advect relatively low PV air southward on the west side of the vortex. The vortex becomes larger by drawing upon the PV of the strip. By 48 h PV from the strip completely surrounds the original vortex and a large spiral band ex-

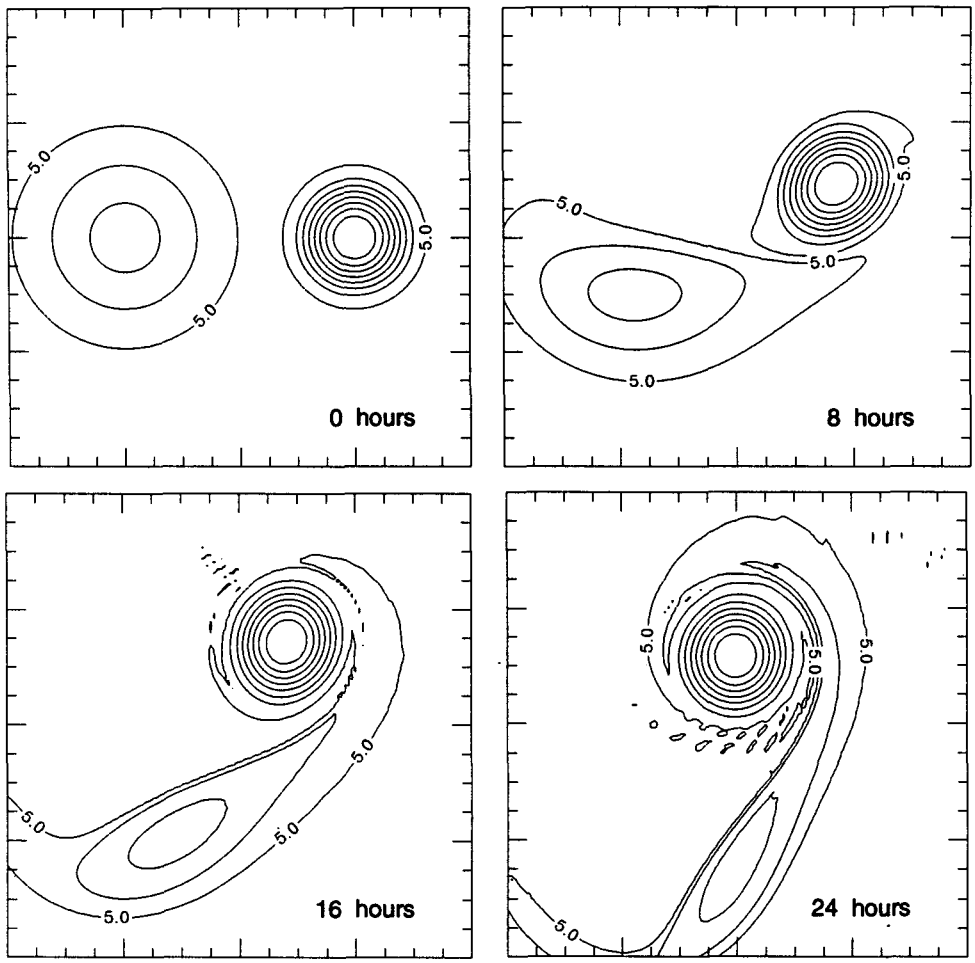

FIG. 10. Experiment 3: merger of a large weak vortex with a small strong vortex. The four panels display the PV field at 0, 8, 16, and 24 h. The initial vorticity field of the small vortex has a maximum value three times that of the larger vortex. Units are 10^{-5} s^{-1}.

tends from the vortex. This result again supports Holland's argument for the development of large tropical cyclones.

b. Diabatic sources away from the cyclone center

In the previous three simulations, we considered the formation of bands from initial states that had two preexisting vortices or regions of PV. In Experiment 5, a single axisymmetric vortex that encounters an area of intense convection is considered (a mass sink in the shallow-water model). The goal is to more closely simulate the actual banding process by convective asymmetries in nature. Because a mass sink is added to the model, the mean depth of the fluid (H) is increased to 2000 m, which allows the model to evolve without encountering any problems associated with massless layers. By increasing the basic-state depth of the fluid, however, we also increase the pure gravity wave speed and therefore the Rossby radius. Model results indicate that these changes have no adverse effects on the simulations.

Our simulation consists of an axisymmetric vortex located north of a large convection area. This area of convection is an ellipse whose center is initially located 400 km south of the vortex center. The elliptical region has a maximum semimajor axis length of 300 km. The heating function is therefore similar in shape (but not size) to the initial vorticity pattern for experiment 1. The maximum value of the mass sink roughly corresponds to a maximum heating rate of ~40–50 K/day. To prevent the excitation of transient gravity waves and ensure evolution along the diabatic slow manifold, the mass sink is turned on slowly over a period of approximately 12 h, after which it is held fixed. The model is integrated using $(128)^2$ points on the transform grid while keeping 42 waves. Results from this simulation are shown in Fig. 12. Initially the vortex was centered in x and located near the top of the figure. The mass sink is also centered in x and is fixed near the bottom

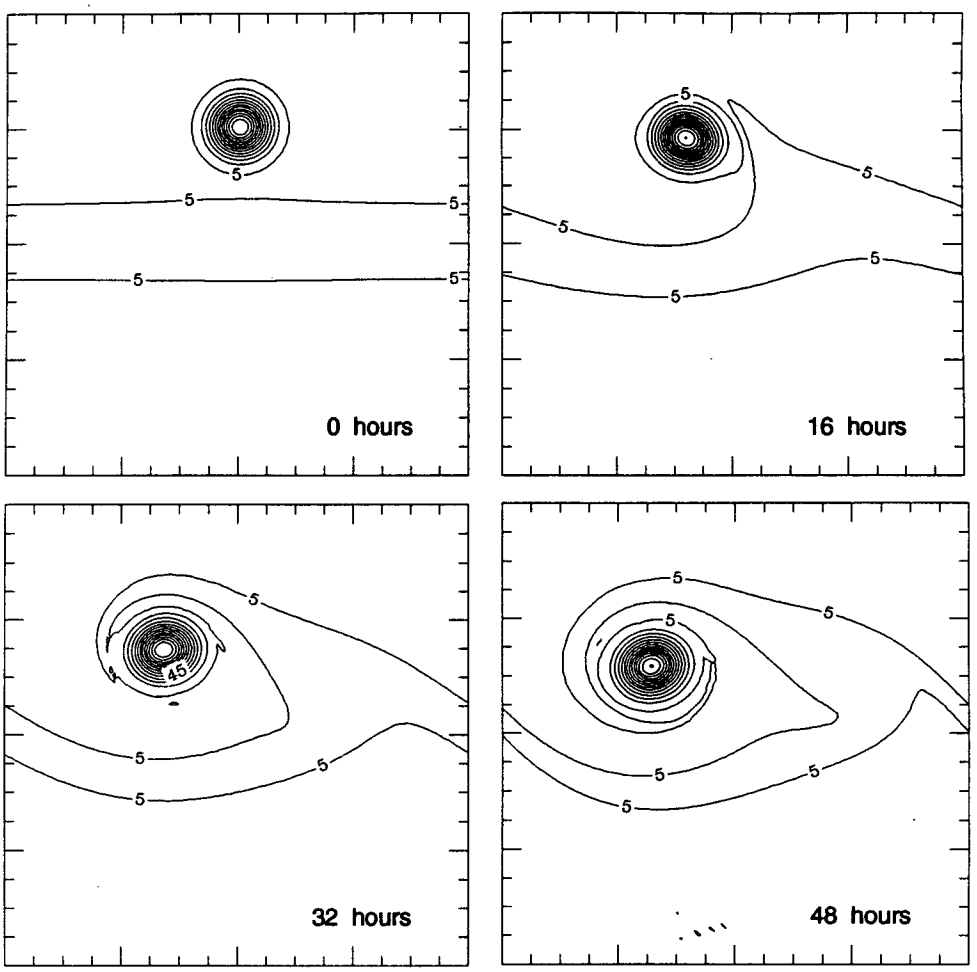

FIG. 11. Experiment 4: interaction of a vortex with a strip of vorticity, such as the ITCZ. The four panels display the PV field at 0, 16, 32, and 48 h. The initial vorticity in the vortex is 6.4 times the vorticity in the strip. Units are 10^{-5} s^{-1}.

of the figure. By 24 h the presence of the mass sink has been felt on the entire eastern edge of the vortex. In addition, the vortex has shifted towards the lower pressure created by the mass sink, moving almost 200 km. The weak cyclonic circulation created by the sink has also caused the vortex to move slightly westward. By 48 h the PV field from the vortex and that due to the mass sink have merged. The result is a large tail of PV extending in a spiral fashion from the southern edge of the vortex. The height field associated with the vortex shows slight asymmetries associated with the spiral band, suggesting the model is evolving near the diabatic slow manifold. The band is also found to correspond to the location of secondary tangential wind maxima. Figure 13 shows the tangential wind speed for four radial arms that emanate from the vortex center. The upper left panel (a radial toward the west of the vortex center) shows clearly that the band is associated with an increase in the tangential wind. These secondary wind maxima [also discussed by Richie and Holland (1993) and Holland and Dietachmayer (1993)] are often found in nature (Willoughby et al. 1982). They were interpreted by Shapiro and Willoughby (1982) as being the balanced model response to an axisymmetric ring of convection (i.e., a concentric eyewall). From the results shown in Figs. 3, 9, 10, 12, and 13 we conclude that such secondary wind maxima can also be produced by wave breaking, merger, and by asymmetric convection whose associated PV anomaly has been elongated and wrapped around the main vortex.

Another interesting feature in the 48-h fields is the formation of what might be considered secondary bands (Willoughby et al. 1984). These bands are especially visible on the northern edge of the vortex and appear to be due the asymmetric mass sink that is now positioned much closer the center of vortex. Beyond 48 h, the vortex begins to rapidly intensify as its position moves nearer to the mass sink. Gradients then become too steep for the model resolution.

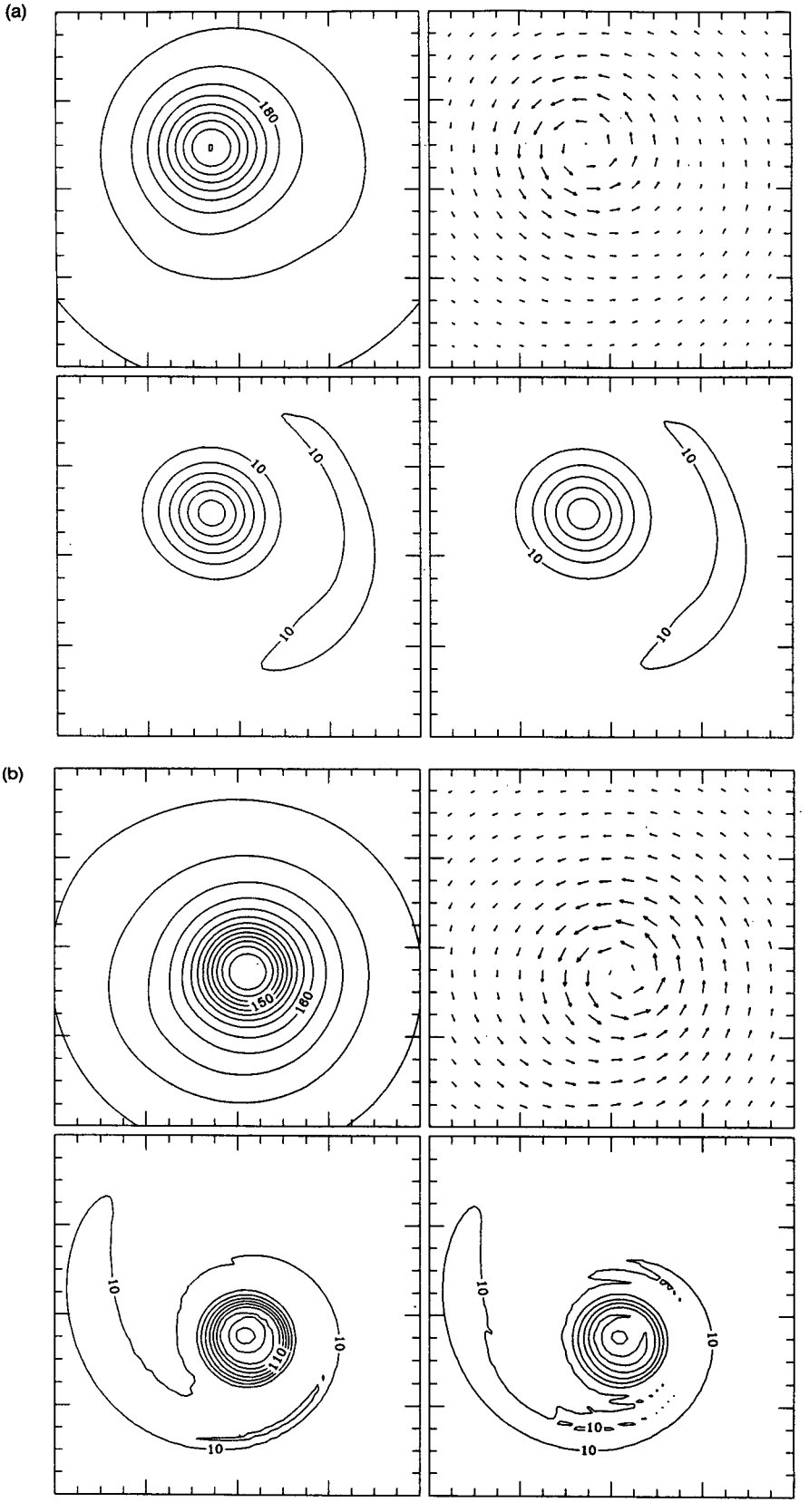

FIG. 12. Experiment 5: asymmetrically heated vortex. The wind and mass fields for the asymmetrically heated vortex at (a) 24 h and (b) 48 h. The height field (upper left) has a contour interval of 2 dm. The maximum wind vector, defined as the distance between two consecutive tick marks, is 50 m s^{-1}. The PV (lower left) and absolute vorticity (lower right) are in units of 10^{-5} s^{-1} and have contour intervals of 2.0×10^{-4}. Only the inner 800 × 800 km of the 1600 × 1600 km domain is shown, with tick marks every 50 km.

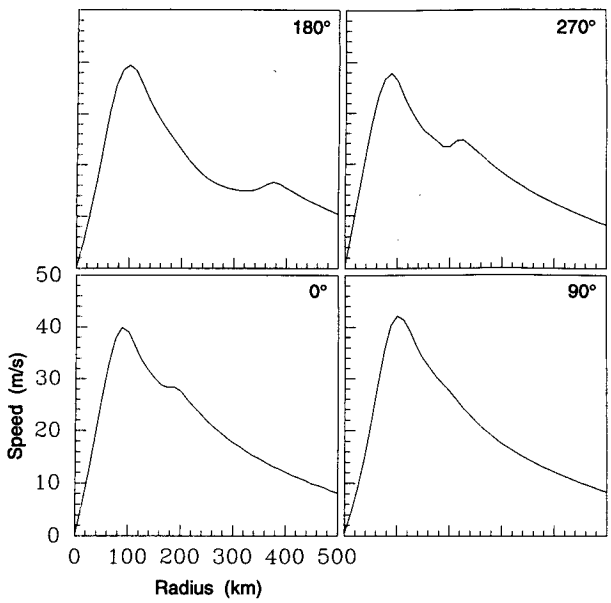

FIG. 13. Tangential winds as a function of radius for experiment 5 at 48 h. The labels on the lower left panel also apply to the other three panels. The upper left panel is along a radial toward the west of the vortex, the upper right panel toward the south, and the lower left panel toward the east; all three cross the band and show secondary wind maxima. The radial toward the north (lower right panel) does not cross the band and does show a secondary wind maximum.

These results seem to indicate that banding processes can be explained rather well using PV arguments. Related experiments (not shown) indicate that other forms of asymmetric heating can also produce concentric eyewalls similar to those observed occasionally in small, intense tropical cyclones. During a model simulation in which the heating was turned off slowly, thus simulating a vortex that comes in contact with an area of intense convection but slowly propagates away, the asymmetries in the PV field simply wrapped around the existing vortex, creating an annular region of PV. The fact that concentric eyewalls are only observed in more intense hurricanes supports this idea. When coming in contact with an area of intense convection, more intense hurricanes would allow the PV anomalies to simply wrap around the vortex before interacting with it. Observational studies would need to be done, however, to support this hypothesis.

4. Band formation through breakdown of the ITCZ

a. *Review of the linear stability analysis for a zonal strip of high vorticity*

When a zonally elongated line of ITCZ convection forms off the equator, a zonally symmetric flow tends to develop. For the case of an ITCZ near 10°N (such as that shown in Fig. 1) low-level easterlies are produced north of the ITCZ while low-level westerlies are produced between the equator and the ITCZ. At upper levels, the zonal flow is just the opposite. The low-level cyclonic shear zone between the easterlies and westerlies (the monsoon trough) can also be envisaged as a zonal strip of uniformly high PV, with large poleward gradients of PV on its edges. On the south edge of the strip the PV increases to the north, while on the north edge the PV decreases to the north. In terms of PV (Rossby) wave theory, a PV wave on the south edge of the strip will propagate westward relative to the westerly flow there, while a PV wave on the north edge will propagate eastward relative to the easterly flow there. Thus, it is possible for these two counterpropagating (relative to the zonal flow in their vicinity) PV waves to have the same phase speed relative to the earth, that is, to be phase locked. If the locked phase is favorable, each PV wave will make the other grow, and barotropic instability will result (Hoskins et al. 1985). This barotropic idealization is one view of the origin of easterly waves. In reality baroclinic and diabatic effects must also be important (after all, the basic-state PV field results from diabatic effects), but here we shall isolate the barotropic processes in order to investigate the extent to which they explain spiral bands.

In order to make the above discussion quantitative, consider a zonal strip of high PV in a nondivergent barotropic model on an infinite f plane (Rayleigh 1945, pp. 392–394; Gill 1982, section 13.6; Dritschel 1989; Pratt and Pedlosky 1991). Since there is no distinction between potential vorticity and vorticity in such a nondivergent model, we can use these terms interchangeably. For the basic-state shear layer defined by

$$\bar{u}(y) = \begin{cases} -\zeta_0 y_0, & y_0 \leqslant y < \infty \\ -\zeta_0 y, & -y_0 \leqslant y \leqslant y_0 \\ \zeta_0 y_0, & -\infty < y \leqslant -y_0, \end{cases} \tag{4.1}$$

the corresponding relative vorticity equals the positive constant ζ_0 in the central region $-y_0 < y < y_0$ and vanishes elsewhere. Now consider small amplitude perturbations of fluid particles on this basic state. Since the basic-state vorticity is piecewise constant, the perturbation vorticity will vanish everywhere except near the edges of the PV strip, that is, $\nabla^2\psi = 0$ for $y \neq \pm y_0$, where ψ is the perturbation streamfunction. For sinusoidal meridional displacements (denoted by η) of the strip edges we have $\eta_n = \hat{\eta}_n e^{i(kx-\sigma t)}$ and $\eta_s = \hat{\eta}_s e^{i(kx-\sigma t)}$, where k is the zonal wavenumber, σ the complex frequency, $\hat{\eta}_n$ and $\hat{\eta}_s$ are complex constants, and the subscripts n and s denote northern and southern edges. The solution is then $\psi = \{\hat{\psi}_n e^{-k|y-y_0|} + \hat{\psi}_s e^{-k|y+y_0|}\} e^{i(kx-\sigma t)}$, where $\hat{\psi}_n$ and $\hat{\psi}_s$ are complex constants. The solution associated with the constant $\hat{\psi}_n$ has PV anomalies concentrated at $y = y_0$ and the corresponding streamfunction decays away from

$y = y_0$. Similarly, the solution associated with $\hat{\psi}_s$ has PV anomalies concentrated at $y = -y_0$ and the corresponding streamfunction decays away from $y = -y_0$. To relate $\hat{\psi}_n$ to $\hat{\eta}_n$ and $\hat{\psi}_s$ to $\hat{\eta}_s$ we require continuity of the total zonal wind at the displaced edges $y = y_0 + \eta_n$ and $y = -y_0 + \eta_s$, which results in $k\hat{\psi}_n = \frac{1}{2}\zeta_0\hat{\eta}_n$ and $k\hat{\psi}_s = -\frac{1}{2}\zeta_0\hat{\eta}_s$. Using these results in the equations $(\partial/\partial t + \bar{u}\partial/\partial x)\eta_n = \partial\psi/\partial x$ at $y = y_0$ and $(\partial/\partial t + \bar{u}\partial/\partial x)\eta_s = \partial\psi/\partial x$ at $y = -y_0$, we obtain the matrix eigenvalue problem

$$\frac{1}{2}\zeta_0\begin{pmatrix}(1-2ky_0) & -e^{-2ky_0}\\ e^{-2ky_0} & -(1-2ky_0)\end{pmatrix}\begin{pmatrix}\hat{\eta}_n\\ \hat{\eta}_s\end{pmatrix} = \sigma\begin{pmatrix}\hat{\eta}_n\\ \hat{\eta}_s\end{pmatrix}, \quad (4.2)$$

which can be regarded as a concise mathematical description of the interaction of two counterpropagating PV waves. If the northern wave were absent, the frequency of the southern wave, determined from the second row of (4.2), would be given by $\sigma/k = \bar{u}(-y_0) - \zeta_0/(2k)$, which represents a PV wave propagating westward relative to the westerly flow at $y = -y_0$. Similarly, if the southern wave were absent, the first row of (4.2) would give $\sigma/k = \bar{u}(y_0) + \zeta_0/(2k)$, which represents a PV wave propagating eastward relative to the easterly flow at $y = y_0$. In the general case, both waves are present (their interaction being represented by the off-diagonal terms in the matrix), and the eigenvalues of (4.2) are given by $\sigma = \pm\frac{1}{2}\zeta_0[(1-2ky_0)^2 - e^{-4ky_0}]^{1/2}$. Pure imaginary σ occurs if $0 \leq ky_0 \leq 0.6392$. The most unstable mode occurs when $ky_0 = 0.3984$, which corresponds to a zonal wavelength approximately eight times the width of the strip. For this most unstable mode, the time behavior is $e^{0.2012\zeta_0 t}$, so that the e-folding time is approximately $5/\zeta_0$. For $\zeta_0 = 6.25 \times 10^{-5}$ s^{-1}, which is the value used in the shallow-water experiment described below, the e-folding time of the most unstable mode is 0.92 days.

b. *Numerical experiment with the nonlinear shallow-water model*

Now let us use the above nondivergent normal-mode stability analysis as a guide in setting up a numerical experiment in our shallow-water model. For this experiment we have chosen a square domain 6400 km on each side with $f = 2.5 \times 10^{-5}$ s^{-1} and $H = 300$ m. As an idealized monsoon trough shear zone let us consider a relative vorticity field that is uniform at 6.25×10^{-5} s^{-1} in the region $3100 \leq y \leq 3300$ km. In the adjacent regions $2800 \leq y \leq 3100$ km and $3300 \leq y \leq 3600$ km the relative vorticity decreases smoothly to a slightly negative value that is maintained over the rest of the domain. The slightly negative relative vorticity outside the strip is required to make the area-averaged relative vorticity vanish. This zonally symmetric vorticity field, along with its associated balanced wind, geopotential, and potential vorticity, is shown in Fig. 14a. The maximum easterly and westerly zonal flows near the north and south edges of the vorticity strip are 11 m s^{-1}, so the total shear across the strip is 22 m s^{-1}. According to the normal-mode stability analysis for piecewise constant vorticity strips in a nondivergent barotropic model, we should expect barotropically unstable waves with a zonal wavelength approximately eight times the width of the strip, that is, approximately a zonal wavenumber 2 pattern. To excite such an instability without causing significant gravity wave motions in the shallow-water model, we have added white noise to the initial rotational mode spectral coefficients while leaving the gravitational mode coefficients undisturbed. This noise field has been scaled in such a way that the initial physical space wind perturbations are typically around 0.01 m s^{-1}. With this weak initial perturbation, the patterns change very slowly at first, but after 8 days a distinct wavenumber two pattern has begun to emerge. By 10 days (Fig. 14b) the patterns are evolving more quickly, and the PV field has taken on a varicose character, with PV beginning to pool in regions connected by filaments. In a sense, the pooled regions are competing with each other to acquire all the potential vorticity in the filaments. By 12 days the pools have become more axisymmetric and the filaments have become elongated and started to wrap around the PV centers. The elongated filaments of PV at 12 days have a similar appearance to the long thin bands of convection in Fig. 1. Thus, outer bands such as those observed in Fig. 1 may be the remnants of those parts of the ITCZ, which have been elongated and coiled by other parts of the ITCZ that have pooled their PV into nearly symmetric vortices. The pooled regions of PV are not yet hurricanes. For them to become hurricanes requires a substantial boost in their PV through diabatic processes. The PV dynamics of this final nonlinear phase has been studied with an axisymmetric balanced vortex model by Schubert and Alworth (1987).

A beautiful example of ITCZ breakdown and the formation of a tropical cyclone has been pointed out to us by Dr. L. Shapiro. The example can be seen in the series of satellite pictures presented by Agee (1972). These show the ITCZ developing a wavy character, a tropical storm forming near a wave crest, and connecting cloud bands joining the ITCZ and the tropical storm at the later stages of development. Shapiro (personal communication) interprets the entire process as a "redistribution of vorticity, associated with the strong shear in the ITCZ, into an isolated vortex." The pooling process illustrated in Fig. 14b entirely supports this interpretation.

In passing, we note that a high-resolution spectral model is not necessary to illustrate the pooling and filamentation processes. In fact, simple nonlinear contour dynamics models with only two contours (three piecewise constant vorticity regions) yield elegant simulations as can be seen in Dritschel (1989, Fig. 3) and Pratt and Pedlosky (1991, Fig. 5).

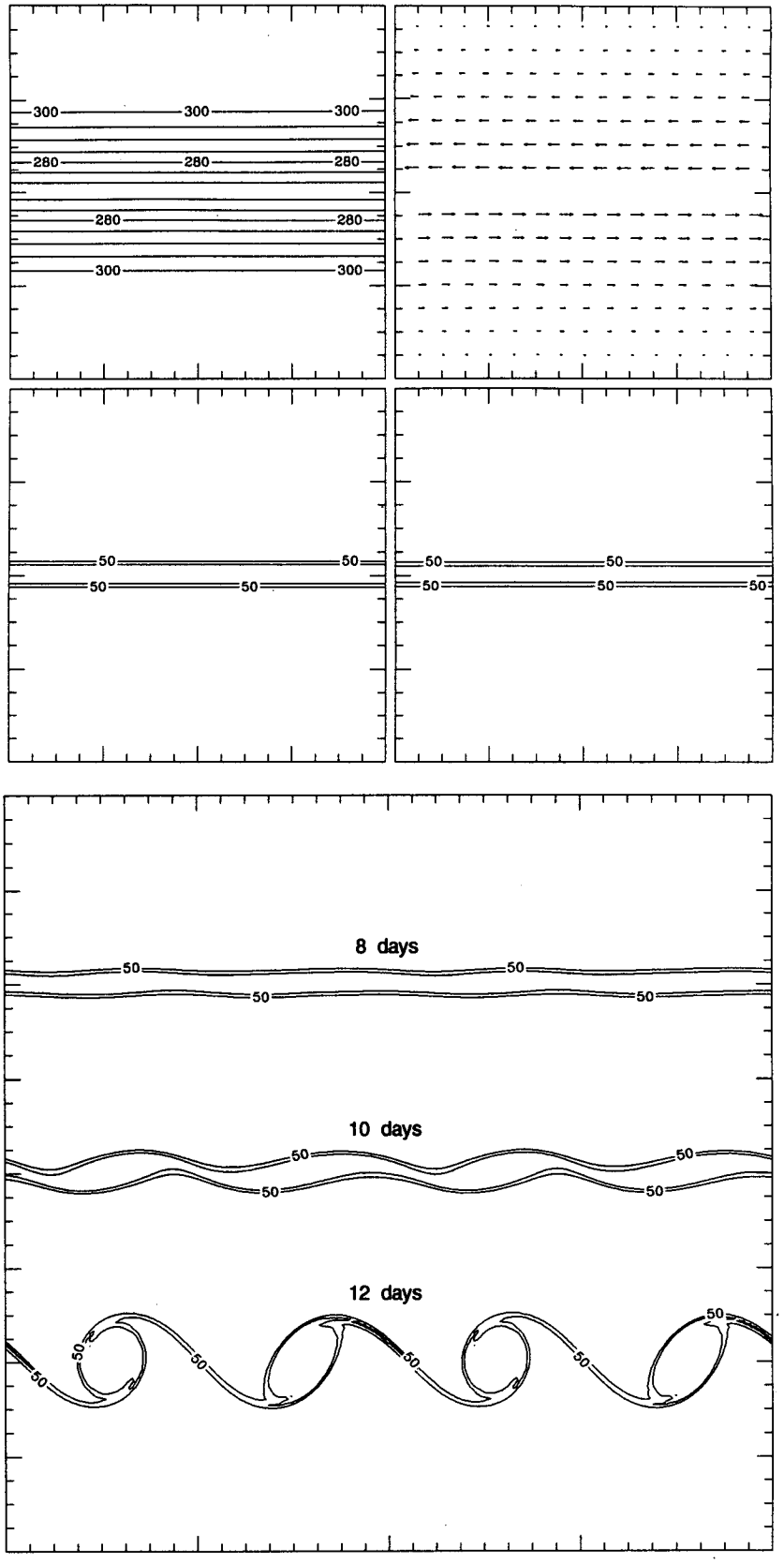

FIG. 14. Experiment 6: formation of bands due to ITCZ breakdown. Dynamic fields (fluid depth, upper left; wind vectors, upper right; potential vorticity, lower left; vorticity, lower right) at initial time (a) and the vorticity field at 8, 10, and 12 days (b). In part (a) the N–S and E–W axes are 6400 km in length, with tick marks every 400 km. In part (b) the tick marks are also every 400 km, but the periodic E–W domain is displayed twice for clarity.

5. Concluding remarks

Moist convective processes near the tropical cyclone center continuously conspire to make high PV there, with asymmetries in the distribution of moist convection resulting in asymmetries in the PV pattern. The PV wave breaking mechanism and the merger mechanism then continuously operate to symmetrize the PV field. In the symmetrization process spiral bands of high PV develop in the surrounding fluid. The region surrounding the high PV core can be expected to take on the surf zone character of two-dimensional turbulence.

Do observations actually reveal a surf zone in hurricanes? Although observationalists have yet to produce fine-grain maps of vorticity or potential vorticity, flight legs routinely produce radial profiles of the tangential wind, which is of course closely related to the vorticity. In mature hurricanes these plots of $v(r)$ often show (e.g., Willoughby et al. 1982, Figs. 2 and 4) a rather smooth character inside approximately 50 km and an irregular or turbulent character outside this radius. This is entirely consistent with the concept of a surf zone outside the high PV vortex core.

In an encounter between two vortices of different PV maxima and different areas, there is often merger and filamentation. One vortex is usually victorious in the sense that its fluid particles (and hence its PV) end up in the central core of the combined vortex, with the PV of the loser elongated and coiled around the victor. A long-lived tropical cyclone can be envisaged as experiencing victory after victory as it coils weaker PV anomalies around itself. If the cyclone does not meet its demise after landfall or recurvature over colder water, there is one last encounter it is likely to loose—its encounter with the tropospheric polar vortex. This occurs when the tropical cyclone, which had been drifting to the northwest, recurves into the midlatitude westerlies and finds itself, an intense but small PV anomaly, up against the less intense but huge polar vortex. In this encounter, the tropical cyclone often gets sheared out into a PV streak and becomes incorporated into the polar vortex. The above process, in which the high PV induced by convection in tropical regions ends up in an elongated form in the polar vortex, can be clearly seen in time lapse geostationary satellite film loops.

Tropical cyclones occur in a wide variety of sizes. A large cyclone and a small cyclone might have nearly the same maximum tangential wind speed near the radius of eyewall convection, but in the small cyclone the wind decreases rapidly with radius while in the large cyclone the wind decreases slowly with radius. The area of gale force winds (i.e., winds greater than 17 m s^{-1}) can differ by over a factor of 100 between large and small cyclones. Since the tangential wind structures can be so different in large and small cyclones, the vorticity and potential vorticity structures can also be quite different, with large cyclones having vorticity and potential vorticity spread over a larger horizontal area. Two possible explanations for these different potential vorticity distributions are as follows. First, the moist convection (which results in high potential vorticity in the lower troposphere) might be distributed differently in large and small cyclones, with a confined, intensely raining area in small cyclones and a broad area of rainfall in large cyclones. A second possibility is that small intense tropical cyclones have developed in a nearly symmetric fashion with minimal vortex merging, while large tropical cyclones have experienced significant merging and growth in the area of high PV. In the latter case, the PV is spread over a much larger area so that significant tangential winds extend out to large radii.

A question sometimes asked (Ryan et al. 1992) is whether rainbands help or hinder the development of the cyclone-scale circulation. The use of terms such as "feeder bands" seems to imply that the bands are helping development by feeding moisture to the mesoscale power plant at the eyewall. The present integrations suggest that PV, in addition to moisture, can be fed into the vortex. Both these effects would appear to help development. In contrast, according to the efficiency analysis of Hack and Schubert (1986), the most rapidly developing cyclones should be those that manage to get nearly all of their latent heat release as close to the eyewall as possible. Since bands tend to cause latent heat release away from the eyewall, they may, in this sense, be regarded as hindering development.

In closing, we would like to note that researchers on middle atmosphere dynamics have significantly advanced their subject by producing global, isentropic maps of PV, both from observations and model output. In a similar way, the construction of observationally based and model-based, fine-grain PV maps for tropical cyclones and the ITCZ could significantly advance our understanding of tropical dynamics.

Acknowledgments. We have benefited greatly from extended discussions with Greg Holland, who has arrived at many similar conclusions through observational experience and experiments with a shallow-water model and a contour dynamics program. We would also like to thank Kerry Emanuel, William Gray, Michael Montgomery, David Randall, and Lloyd Shapiro for their helpful comments. The work of T. Guinn has been supported by the United States Air Force through the AFIT Program. The work of W. Schubert has been supported by the Office of Naval Research under Grant N000014-88-K-0214.

APPENDIX A

Normal-Mode Model

To derive the normal-mode model, let us first write (1.1)–(1.3) in the vector form

$$\frac{\partial \mathbf{W}}{\partial t} + \mathcal{L}\mathbf{W} = \mathbf{N} + \mathbf{F}, \tag{A.1}$$

where $\mathbf{W} = [u, v, \Phi/c]^{\mathrm{T}}$ with $\Phi = g(h - H)$ the deviation geopotential; $\mathbf{N} = [\zeta v - \partial K/\partial x, -\zeta u - \partial K/\partial y, -\partial(u\Phi/c)/\partial x - \partial(v\Phi/c)/\partial y]^{\mathrm{T}}$ represents the nonlinear terms with $K = \frac{1}{2}(u^2 + v^2)$ the kinetic energy and $\zeta = \partial v/\partial x - \partial u/\partial y$ the relative vorticity; $\mathbf{F} = [F, G, gS/c]^{\mathrm{T}}$ represents the forcing terms; and the linear operator $\mathcal{L}$ is defined by

$$\mathcal{L} = \begin{pmatrix} 0 & -f & c\partial/\partial x \\ f & 0 & c\partial/\partial y \\ c\partial/\partial x & c\partial/\partial y & 0 \end{pmatrix}.$$

Now define the inner product of any complex three component vectors $\mathbf{f}$ and $\mathbf{g}$ by

$$(\mathbf{f}, \mathbf{g}) = \frac{1}{L_x L_y}\int_0^{L_x}\int_0^{L_y}(f_1 g_1^* + f_2 g_2^* + f_3 g_3^*)\,dx\,dy, \tag{A.2}$$

where $*$ denotes the complex conjugate. The operator $\mathcal{L}$ is skew-Hermitian with respect to the inner product (A.2), which guarantees that the eigenvalues of $\mathcal{L}$ are pure imaginary and the eigenfunctions are orthogonal (as long as degeneracy does not occur). The eigenvalues will be denoted by $i\nu_{mnq}$ and the eigenfunctions by $\mathbf{K}_{mnq}(x, y)$, so that $\mathbf{K}_{mnq}$ satisfies $\mathcal{L}\mathbf{K}_{mnq} = i\nu_{mnq}\mathbf{K}_{mnq}$, where (mnq) are integers that, respectively, index the wavenumber in x, the wavenumber in y, and the three different eigenvalues and eigenfunctions for a given (mn). The eigenvalues are given by

$$\nu_{mnq} = \begin{cases} 0, & q = 0 \quad \text{(rotational modes)} \\ (-1)^q \nu_{mn}, & q = 1, 2 \quad \text{(gravitational modes)}, \end{cases}$$

and the corresponding eigenfunctions by

$$\mathbf{K}_{mnq}(x, y) = e^{i(k_m x + l_n y)} \times \begin{cases} \dfrac{1}{\nu_{mn}}\begin{pmatrix} -icl_n \\ ick_m \\ f \end{pmatrix} & q = 0 \\ \dfrac{1}{\sqrt{2}\mu_{mn}\nu_{mn}}\begin{pmatrix} \nu_{mnq}k_m + ifl_n \\ \nu_{mnq}l_n - ifk_m \\ c\mu_{mn}^2 \end{pmatrix} & q = 1, 2 \end{cases}, \tag{A.3}$$

where $\nu_{mn} = (f^2 + c^2\mu_{mn}^2)^{1/2}$, $\mu_{mn} = (k_m^2 + l_n^2)^{1/2}$, $k_m = 2\pi m/L_x$, and $l_n = 2\pi n/L_y$.

It can be easily shown that the eigenfunctions given by (A.3) are orthonormal, that is,

$$(\mathbf{K}_{mnq}, \mathbf{K}_{m'n'q'}) = \begin{cases} 1, & \text{if } (m, n, q) = (m', n', q') \\ 0, & \text{otherwise.} \end{cases} \tag{A.4}$$

Because the eigenfunctions $\mathbf{K}_{mnq}(x, y)$ form a complete set, our original dependent variables $\mathbf{W}(x, y, t)$ can be expressed as the series

$$\mathbf{W}(x, y, t) = \sum_{mnq} W_{mnq}(t)\mathbf{K}_{mnq}(x, y), \tag{A.5}$$

where $W_{mnq}(t)$ is the complex scalar spectral coefficient. Taking the inner product of (A.5) with $\mathbf{K}_{m'n'q'}$ and using the orthonormality relation (A.4),

$$W_{mnq}(t) = (\mathbf{W}(x, y, t), \mathbf{K}_{mnq}(x, y)) \tag{A.6}$$

is obtained. The relations (A.5) and (A.6) can be regarded as a normal-mode transform pair, with (A.6) giving the transformation from physical space to normal-mode spectral space and (A.5) giving the transformation from normal-mode spectral space to physical space.

To transform our original shallow-water equations, we take the inner product of (A.1) with $\mathbf{K}_{mnq}(x, y)$ to obtain

$$\frac{\partial}{\partial t}(\mathbf{W}, \mathbf{K}_{mnq}) + (\mathcal{L}\mathbf{W}, \mathbf{K}_{mnq}) = (\mathbf{N}, \mathbf{K}_{mnq}) + (\mathbf{F}, \mathbf{K}_{mnq}).$$

Using (A.6) and the fact that $(\mathcal{L}\mathbf{W}, \mathbf{K}_{mnq}) = -(\mathbf{W}, \mathcal{L}\mathbf{K}_{mnq}) = i\nu_{mnq}(\mathbf{W}, \mathbf{K}_{mnq})$, we obtain

$$\frac{dW_{mnq}}{dt} + i\nu_{mnq}W_{mnq} = N_{mnq} + F_{mnq}, \tag{A.7}$$

where $N_{mnq} = (\mathbf{N}, \mathbf{K}_{mnq})$ and $F_{mnq} = (\mathbf{F}, \mathbf{K}_{mnq})$. We have now transformed our original governing system (A.1) into the spectral equations (A.7).

The solutions presented in this paper were obtained by numerically solving (A.7) with the nonlinear terms calculated using an alias-free transform method, that is, by transforming to physical space each time step via (A.5), calculating the nonlinear terms in physical space, and then transforming to N_{mnq} so that (A.7) can be stepped forward in time.

It is important to note that the method yields a natural partitioning of the solution into rotational and gravitational parts. To obtain the contribution due to rotational modes we sum (A.5) over all m and n but only over $q = 0$. Similarly, to obtain the contribution due to gravitational modes, (A.5) is summed over all m and n but only over $q = 1$ and $q = 2$.

APPENDIX B

Wave Activity Diagnostics

It is often convenient to decompose an atmospheric flow into a basic state and a disturbance to that basic state. After making this decomposition of the flow, it is possible to derive wave activity conservation laws. Wave activity is a conserved disturbance quantity that is of quadratic or higher order in the small amplitude limit. In this Appendix, we follow the approach of Haynes (1988) in deriving a finite-amplitude wave activity conservation relation for the adiabatic, frictionless version of the shallow-water equations.

For convenience we now use cylindrical coordinates and denote the radial component of velocity by u and the tangential component by v. Thus, our decomposition of the total flow is $u = u_0 + u_e$, $v = v_0 + v_e$, $h = h_0 + h_e$, where the subscript $_0$ denotes basic state and the subscript $_e$ denotes disturbance or eddy. No linearization is used so the variables with subscript $_e$ can be of any magnitude. The basic state chosen here is one with zero radial component (i.e., $u_0 = 0$), a tangential component $v_0(r)$ obtained by taking the tangential average of the initial condition, and a depth $h_0(r)$ that is in gradient balance with $v_0(r)$. This basic state is a steady, symmetric solution of the original equations.

To derive the wave activity relation we begin with the governing equations in the form

$$\frac{\partial(hu)}{\partial t} + \frac{\partial(rhuu)}{r\partial r} + \frac{\partial(hvu)}{r\partial\phi} - \left(f + \frac{v}{r}\right)hv + gh\frac{\partial h}{\partial r} = 0, \quad \text{(B.1)}$$

$$\frac{\partial[h(rv + \frac{1}{2}fr^2)]}{\partial t} + \frac{\partial[rhu(rv + \frac{1}{2}fr^2)]}{r\partial r} + \frac{\partial[hv(rv + \frac{1}{2}fr^2)]}{r\partial\phi} + gh\frac{\partial h}{\partial\phi} = 0, \quad \text{(B.2)}$$

$$\frac{\partial h}{\partial t} + \frac{\partial(rhu)}{r\partial r} + \frac{\partial(hv)}{r\partial\phi} = 0, \quad \text{(B.3)}$$

where h is the fluid depth. Equations (B.1)–(B.3) are regarded as a closed system in u, v, and h. A consequence of (B.1)–(B.3) is the conservation of the potential vorticity P. Since P is conserved, any function $C(P)$ is also conserved. Thus, the Casimir function $C(P)$ satisfies

$$\frac{\partial(hC)}{\partial t} + \frac{\partial(ruhC)}{r\partial r} + \frac{\partial(vhC)}{r\partial\phi} = 0. \quad \text{(B.4)}$$

Adding (B.2) and (B.4), we obtain

$$\frac{\partial[h(rv + \frac{1}{2}fr^2 + C)]}{\partial t} + \frac{\partial[ruh(rv + \frac{1}{2}fr^2 + C)]}{r\partial r} + \frac{\partial[vh(rv + \frac{1}{2}fr^2 + C) + r\frac{1}{2}gh^2]}{r\partial\phi} = 0. \quad \text{(B.5)}$$

Following Haynes (1988), $C(P)$ is chosen such that the disturbance part of $h(rv + \frac{1}{2}fr^2 + C)$ can be written as a divergence, plus a term that is explicitly second order in wave amplitude. The disturbance part of $h(rv + \frac{1}{2}fr^2 + C)$ is defined as

$$\left\{h\left[rv + \frac{1}{2}fr^2 + C(P)\right]\right\}_e = h\left[rv + \frac{1}{2}fr^2 + C(P)\right] - h_0\left[rv_0 + \frac{1}{2}fr^2 + C(P_0)\right].$$

After some manipulation, this can be written

$$\left\{h\left[rv + \frac{1}{2}fr^2 + C(P)\right]\right\}_e = rv_eh_e + h[C(P) - C(P_0) - P_eC'(P_0)] + \frac{\partial[C'(P_0)rv_e]}{r\partial r} - \frac{\partial[C'(P_0)u_e]}{r\partial\phi} + h_e\left[rv_0 + \frac{1}{2}fr^2 + C(P_0) - P_0C'(P_0)\right] + rv_e\left[h_0 - \frac{\partial C'(P_0)}{r\partial r}\right]. \quad \text{(B.6)}$$

The first line on the right-hand side of (B.6) is second order in the disturbance amplitude and will turn out to be the wave activity. The second line is the divergence of a flux. Now choose $C(P)$ in such a way that the last two lines in (B.6) vanish. The choice

$$C(P) = -\int_P^{P_{\max}} m(\tilde{P})d\tilde{P}, \quad \text{(B.7)}$$

where

$$m(P_0(r)) = \int_0^r h_0(\tilde{r})\tilde{r}d\tilde{r}, \quad \text{(B.8)}$$

makes the last term in the square brackets in (B.6) vanish, as can easily be verified. Since

$$\frac{\partial}{r\partial r}\left[rv_0 + \frac{1}{2}fr^2 + C(P_0) - P_0C'(P_0)\right] = P_0\left[h_0 - \frac{\partial C'(P_0)}{r\partial r}\right], \quad \text{(B.9)}$$

and since the right-hand side of (B.9) vanishes by the previous argument, we conclude that $rv_0 + \frac{1}{2}fr^2 + C(P_0) - P_0C'(P_0) = \text{const}$. The constant is zero because the left-hand side vanishes at $r = 0$. Thus, the last two lines in (B.6) vanish, and we write (B.6) as

$$\left\{h\left[rv + \frac{1}{2}fr^2 + C(P)\right]\right\}_e = A + \frac{\partial[m(P_0)rv_e]}{r\partial r} - \frac{\partial[m(P_0)u_e]}{r\partial\phi}, \quad \text{(B.10)}$$

where

$$A = rv_eh_e + h[C(P) - C(P_0) - P_em(P_0)] \quad \text{(B.11)}$$

is the wave activity.

Noting that the basic state is a steady solution of the governing equations and then substituting (B.10) into (B.5), we obtain

$$\frac{\partial A}{\partial t} + \frac{\partial}{r\partial r}\left[hru\left(rv + \frac{1}{2}fr^2 + C\right) + m(P_0)\frac{\partial(rv_e)}{\partial t}\right] + \frac{\partial}{r\partial\phi}\left[hv\left(rv + \frac{1}{2}fr^2 + C\right) + \frac{1}{2}grh^2 - m(P_0)\frac{\partial u_e}{\partial t}\right] = 0. \quad \text{(B.12)}$$

Using the disturbance momentum equations

$$\frac{\partial u_e}{\partial t} - hPv + h_0P_0v_0 + \frac{\partial\left(gh_e + \frac{1}{2}u_e^2 + \frac{1}{2}v^2 - \frac{1}{2}v_0^2\right)}{\partial r} = 0, \quad \text{(B.13)}$$

$$\frac{\partial(rv_e)}{\partial t} + hPru + \frac{\partial\left(gh + \frac{1}{2}u^2 + v_0v_e + \frac{1}{2}v_e^2\right)}{\partial\phi} = 0, \quad \text{(B.14)}$$

in (B.12), we obtain

$$\frac{\partial A}{\partial t} + \frac{\partial[r(uA + h_0ru_ev_e)]}{r\partial r} + \frac{\partial\left[vA + h_0r\frac{1}{2}(v_e^2 - u_e^2) + r\frac{1}{2}gh_e^2\right]}{r\partial\phi} = 0 \quad \text{(B.15a)}$$

with the wave activity (B.11) rewritten as

$$A = rv_eh_e + h\int_{P_0}^{P}[m(\tilde{P}) - m(P_0)]d\tilde{P}, \quad \text{(B.15b)}$$

where

$$m(P_0(r)) = \int_0^r h_0(\tilde{r})\tilde{r}d\tilde{r}. \quad \text{(B.15c)}$$

The relations (B.15) allow us to diagnostically analyze the shallow-water model results in terms of wave activity and its flux. To accomplish this, partition the solution at any particular time into basic state and disturbance parts, and then use (B.15b,c) to compute A and (B.15a) to compute the flux of A.

For the wave breaking experiment shown in Fig. 3, the wave activity and its flux at 4-h intervals are shown in Fig. 5. Initially there are four centers of wave activity—two on the major axis and two on the minor axis of the ellipse. The initial wave activity centered on the minor axis is elongated along the flow vectors and rotates with relatively little change in shape during 12 h. In contrast, the wave activity centered on the major axis is influenced by the differential rotation of the flux vectors, the result of which is an outward movement and spiral banding of this wave activity.

REFERENCES

Agee, E., 1972: Note on ITCZ wave disturbances and formation of tropical storm Anna. *Mon. Wea. Rev.*, **100,** 733–737.

Anthes, R. A., 1982: *Tropical cyclones—Their Evolution, Structure, and Effects. Meteor. Monogr.*, **19,** Amer. Meteor. Soc., 1–208.

Deem, G. S., and N. J. Zabusky, 1978a: Vortex waves: Stationary V-states, interactions, recurrence, and breaking. *Phys. Rev. Lett.*, **40,** 859–862.

——, and ——, 1978b: Stationary V-states, interactions, recurrence, and breaking. *Solitons in Action,* K. Longren and A. Scott, Eds., Academic Press, 277–293.

DeMaria, M., and W. H. Schubert, 1984: Experiments with a spectral tropical cyclone model. *J. Atmos. Sci.*, **41,** 901–924.

Dritschel, D. G., 1989: On the stabilization of a two-dimensional vortex strip by adverse shear. *J. Fluid Mech.*, **206,** 193–221.

——, P. H. Haynes, M. N. Juckes, and T. G. Shepherd, 1991: The stability of a two-dimensional vorticity filament under uniform strain. *J. Fluid Mech.*, **230,** 647–665.

Elsberry, R. L., W. M. Frank, G. J. Holland, J. D. Jarrell, and R. L. Southern, 1987: *A Global View of Tropical Cyclones.* University of Chicago Press, 185 pp.

Fornberg, B., 1977: A numerical study of 2-D turbulence. *J. Comput. Phys.*, **25,** 1–31.

Fujiwhara, S., 1923: On the growth and decay of vortical systems. *Quart. J. Roy. Meteor. Soc.*, **49,** 75–104.

Fung, I. Y.-S., 1977: The organization of spiral rain bands in a hurricane. Ph.D. thesis, Massachusetts Institute of Technology, 139 pp.

Gill, A. E., 1982: *Atmosphere–Ocean Dynamics.* Academic Press, 662 pp.

Gray, W. M., 1964: On the scales of motion and internal stress of the hurricane. Ph.D. dissertation, University of Chicago, 203 pp. [Available from Dept. of Geophysical Sciences, University of Chicago, 5734 S. Ellis Ave., Chicago, IL 60637.]

Griffiths, R. W., and E. J. Hopfinger, 1987: Coalescing of geostrophic vortices. *J. Fluid Mech.*, **178,** 73–97.

Hack, J. J., and W. H. Schubert, 1986: Nonlinear response of atmospheric vortices to heating by organized cumulus convection. *J. Atmos. Sci.*, **43,** 1559–1573.

Haynes, P. H., 1988: Forced, dissipative generalizations of finite-amplitude wave activity conservation relations for zonal and nonzonal basic flows. *J. Atmos. Sci.*, **45,** 2352–2362.

Holland, G. J., and G. Dietachmayer, 1993: On the interaction of tropical cyclone scale vortices. Part III: Continuous barotropic vortices. *Quart. J. Roy. Meteor. Soc.*, **119,** in press.

——, and M. Lander, 1993: The meandering nature of tropical cyclone tracks. *J. Atmos. Sci.*, **50,** 1254–1266.

Hoskins, B. J., M. E. McIntyre, and A. W. Robertson, 1985: On the use and significance of isentropic potential vorticity maps. *Quart. J. Roy. Meteor. Soc.*, **111,** 877–946.

Juckes, M. N., and M. E. McIntyre, 1987: A high-resolution, one-layer model of breaking planetary waves in the stratosphere. *Nature,* **328,** 590–596.

Kurihara, Y., 1976: On the development of spiral bands in a tropical cyclone. *J. Atmos. Sci.*, **33,** 940–958.

Lamb, H., 1932: *Hydrodynamics,* sixth ed., Dover, 732 pp.

Lander, M., and G. J. Holland, 1993: On the interaction of tropical cyclone scale vortices. I. Observations. *Quart. J. Roy. Meteor. Soc.*, **119,** in press.

Leith, C., 1980: Nonlinear normal mode initialization and quasi-geostrophic theory. *J. Atmos. Sci.*, **37,** 958–968.

Lewis, B. M., and H. F. Hawkins, 1982: Polygonal eye walls and rainbands in hurricanes. *Bull. Amer. Meteor. Soc.*, **63,** 1294–1300.

MacDonald, N. J., 1968: The evidence for the existence of Rossby-like waves in the hurricane vortex. *Tellus,* **20,** 138–150.

McIntyre, M. E., and T. N. Palmer, 1984: The 'surf zone' in the stratosphere. *J. Atmos. Terr. Phys.*, **46,** 825–850.

——, and ——, 1985: A note on the general concept of wave breaking for Rossby and gravity waves. *Pure Appl. Geophys.*, **123,** 964–975.

McWilliams, J. C., 1984: The emergence of isolated coherent vortices in turbulent flow. *J. Fluid Mech.*, **146,** 21–43.

Melander, M. V., J. C. McWilliams, and N. J. Zabusky, 1987a: Axisymmetrization and vorticity-gradient intensification of an isolated two-dimensional vortex through filamentation. *J. Fluid Mech.*, **178,** 137–159.

——, N. J. Zabusky, and J. C. McWilliams, 1987b: Asymmetric vortex merger in two dimensions: Which vortex is "victorious?" *Phys. Fluids,* **30,** 2610–2612 (see also the color plate on p. 2604).

——, ——, and ——, 1988: Symmetric vortex merger in two dimensions: Causes and conditions. *J. Fluid Mech.*, **195,** 303–340.

Merrill, R. T., 1984: A comparison of large and small tropical cyclones. *Mon. Wea. Rev.*, **112,** 1408–1418.

Platzman, G., 1968: The Rossby wave. *Quart. J. Roy. Meteor. Soc.*, **94,** 225–248.

Polvani, L. M., and R. A. Plumb, 1992: Rossby wave breaking, microbreaking, filamentation, and secondary vortex formation: The dynamics of a perturbed vortex. *J. Atmos. Sci.*, **49,** 462–476.

——, N. J. Zabusky, and G. R. Flierl, 1989: Filamentation of coherent vortex structures via separatrix crossing: A quantitative estimate of onset time. *Phys. Fluids A,* **1,** 181–184.

Pratt, L. J., and J. Pedlosky, 1991: Linear and nonlinear barotropic instability of geostrophic shear layers. *J. Fluid Mech.*, **224,** 49–76.

Rayleigh, J. W. S., 1945: *The Theory of Sound, Vol. II.* Dover, (reprint of 1894 edition), 504 pp.

Richie, E., and G. J. Holland, 1993: On the interaction of tropical cyclone scale vortices. II. Discrete vortex patches. *Quart. J. Roy. Meteor. Soc.*, **119,** in press.

Rossby, C.-G., 1939: Relation between variations in the intensity of the zonal circulation of the atmosphere and the displacements of the semi-permanent centers of action. *J. Mar. Res.*, **2,** 38–55.

Ryan, B. F., G. M. Barnes, and E. J. Zipser, 1992: A wide rainband in a developing tropical cyclone. *Mon. Wea. Rev.*, **120,** 431–447.

Schubert, W. H., and M. DeMaria, 1985: Axisymmetric, primitive equation, spectral tropical cyclone model. Part I: Formulation. *J. Atmos. Sci.*, **42,** 1213–1224.

——, and B. T. Alworth, 1987: Evolution of potential vorticity in tropical cyclones. *Quart. J. Roy. Meteor. Soc.*, **113,** 147–162.

Shapiro, L. J., 1983: The asymmetric boundary layer flow under a translating hurricane. *J. Atmos. Sci.*, **40,** 1984–1998.

——, 1992: Hurricane vortex motion and evolution in a three-layer model. *J. Atmos. Sci.*, **49,** 140–153.

——, and H. E. Willoughby, 1982: The response of balanced hurricanes to local sources of heat and momentum. *J. Atmos. Sci.*, **39,** 378–394.

Thomson, W., 1880: Vibrations of a columnar vortex. *Phil. Mag.*, **10,** 155–168.

Waugh, D. W., and D. G. Dritschel, 1991: The stability of filamentary vorticity in two-dimensional geophysical vortex-dynamics models. *J. Fluid Mech.*, **231,** 575–598.

Willoughby, H. E., 1978: A possible mechanism for the formation of hurricane rainbands. *J. Atmos. Sci.*, **35,** 838–848.

——, 1988: The dynamics of the tropical cyclone core. *Aust. Meteor. Mag.*, **36,** 183–191.

——, J. A. Clos, and M. G. Shoreibah, 1982: Concentric eye walls, secondary wind maxima, and the evolution of the hurricane vortex. *J. Atmos. Sci.*, **39,** 395–411.

——, F. D. Marks, Jr., and R. J. Feinberg, 1984: Stationary and moving convective bands in hurricanes. *J. Atmos. Sci.*, **41,** 3189–3211.

Zabusky, N. J., M. H. Hughes, and K. V. Roberts, 1979: Contour dynamics for the Euler equations in two dimensions. *J. Comput. Phys.*, **30,** 96–106.